

## Research Article

# Estimation of Reservoir Bio-Optical Water Quality Parameters Using Smartphone Sensor Apps and Landsat ETM+: Review and Comparative Experimental Results

Yashon O. Ouma , J. Waga, M. Okech, O. Lavisa, and D. Mbutia

Department of Civil Engineering, School of Engineering, Moi University, Eldoret, Kenya

Correspondence should be addressed to Yashon O. Ouma; yashon\_o@hotmail.com

Received 22 February 2018; Revised 3 June 2018; Accepted 20 June 2018; Published 6 August 2018

Academic Editor: Fanli Meng

Copyright © 2018 Yashon O. Ouma et al. This is an open access article distributed under the Creative Commons Attribution License, which permits unrestricted use, distribution, and reproduction in any medium, provided the original work is properly cited.

This study presents a comparative evaluation of three real-time imaging-based approaches for the prediction of optically active water constituents as chlorophyll-*a* (Chl-*a*), turbidity, suspended particulate matter (SPM), and reservoir water colour. The imaging models comprise of Landsat ETM+-visible and NIR (VNIR) data and EyeOnWater and HydroColor Smartphone sensor apps. To estimate the selected water quality parameters (WQP) from Landsat ETM+-VNIR, predictive models based on empirical relationships were developed. From the in situ measurements and the Landsat regression models, the results from the remote reflectances of ETM+ green, blue, and NIR independently yielded the best fits for the respective predictions of Chl-*a*, turbidity, and SPM. The concentration of Chl-*a* was derived from the Landsat ETM+ and HydroColor with respective Pearson correlation coefficients  $r$  of 0.8977 and 0.8310. The degree of turbidity was determined from Landsat, EyeOnWater, and HydroColor with respective  $r$  values of 0.9628, 0.819, and 0.8405. From the same models, the retrieved SPM was regressed with the laboratory measurements with  $r$  value results of 0.6808, 0.7315, and 0.8637, respectively, from Landsat ETM+, EyeOnWater, and HydroColor. The empirical study results showed that the imaging models can be effectively applied in the estimation of the physical WQP.

## 1. Introduction

For sustainable water supplies, there is a need for the continuous monitoring of the quality of existing and available water resources. The reason for this is that the quality of surface water is continuously deteriorating, due in part to the growing population and related activities such as increasing urbanization and industrial and agricultural growth. As such, inland water bodies, especially lakes and reservoirs, are confronted with increasing water demand and are consequently facing extensive anthropogenic inputs of nutrients and sediments [1]. In order to address this phenomenon, it is becoming imperative that water quality assessment, planning, and management should be carried out. In this process of water resource sustainable management, routine and accurate water quality monitoring plays a significant role [2, 3].

The conventional water quality assessment via in situ sampling and laboratory measurement methods comprise of the analysis of physical, chemical, and biological properties and indicators. However, the in situ water sampling and the subsequent measurements of water quality parameters (WQP) are only able to represent point-based estimates of the quality of water conditions in time and space, and therefore, obtaining spatial-temporal variations of water quality indices in large water bodies is almost impossible due mostly to cost limitations [4]. Besides being time-consuming, labor-intensive, and costly, some of the significant limitations associated with conventional methods for water quality assessment also includes the inability to monitor, forecast, and manage the entire water body due to the water surface extent and its topographic characteristics and the lack of spatial-temporal data. Secondly is the fact that both the errors

associated with field sampling and laboratory measurement may actually contribute to inaccuracy and low precision of the in situ data analysis results. In order to overcome these limitations, there is need for fast, inexpensive, simple, automated, and noninvasive technology in operational and productive aquatic environmental monitoring [5]. Measurements and observations taken with such tools should provide essential information with respect to biogeophysical water quality aspects [5], in a fashion that is routinely available and economical, and with adequate spatial coverage and spatial resolution.

The reflectance of surface water bodies like reservoir and lakes is directly related to the particulate and dissolved material in the water column. This implies that the intrinsic colour of natural waters is determined by the spectral characteristics and the concentrations of dissolved and suspended coloured compounds. As such, information regarding the water quality status, in terms of the light or transparency and colour, is important in understanding and determining the condition and changes in the aquatic environments. Significantly, there are three main components that alter the colour and influence the transparency of water bodies [6]: (i) coloured dissolved organic matter, (ii) sediment load (total suspended material), and (iii) gross biological activity generally estimated through the chlorophyll concentration.

The apparent colour of natural waters is an aspect of the aquatic environment that can easily be detected and is an essential complementary optical water quality indicator. It has been indicated that the apparent colour of water or the obtained optical measurements are directly proportional to these water quality variables (e.g., [2, 7]). The primary colour-producing agents include the optically active constituents such as inorganic suspended particulate material (SPM or mineral solids), particulate organic matter (POM or phytoplankton chlorophyll-*a* concentration (Chl-*a*) which is the most abundant pigment), and coloured dissolved organic matter (CDOM), also called gelbstoff. The concentration of suspended particulate matter has a large influence on the reflectance of a water body, and the magnitude of the backscattering coefficient will have a direct nonlinear effect on the reflectance. Therefrom, the physical, chemical, and biological properties and indicators of water can be derived directly and or indirectly.

On the other hand, the presence of chlorophyll-*a* (Chl-*a*), an optically active water constituent, indicates the trophic state of a water body, since it acts as the link between nutrient concentration, particularly phosphorus, and algal production. Chl-*a* reflects green, because it absorbs most energy from wavelengths of violet-blue and orange-red light, whose reflectance causes chlorophyll to appear green. Several studies have demonstrated that an increase in Chl-*a* concentration results in a decrease in the spectral response at short wavelengths, particularly in the blue band (e.g., [8, 9]). While turbidity is an optical property of water which scatters and absorbs the light rather than transmit it in straight lines, suspended sediments are responsible for most of the scattering, whereas the absorption is controlled by the presence of Chl-*a* and coloured dissolved or particulate matter [10]. As water turbidity is mainly the result of the presence of

suspended matter, turbidity measurement is often used to calculate fluvial suspended sediment concentrations and is commonly regarded as the opposite of clarity [11].

By using remote sensing, the optically active water constituents can be detected based on their interaction with light and the subsequent change in the energy of the incident radiation as reflected from the water body [4]. The principle of the detection of water quality parameters using imaging is based on the fact that pollutants in water scatter and absorb the incoming solar radiation, and the quality of water can be correlated with the optical characteristics of the water columns, such as colour and transparency [12]. This means that optical data can provide an alternative means for obtaining relatively low-cost and simultaneous information on surface water quality conditions [13, 14]. Despite the ability of remote sensing to be used for the assessment of water quality with the desired advantages of being timely and cost-effective, the technique in itself may not be sufficiently precise and must be benchmarked with the traditional sampling methods and field surveys. That is, for a better insight, an integrated use of remote sensing, in situ measurements, and computer water quality modelling is likely to result into a more robust knowledge of the water quality in a given surface water system [2].

In situ methods, including sampling and field measurements, have for so long been the standard techniques applied in the determination of water quality variables, whereby various tests have been carried out for the estimation of different variables, in different case studies using different methodology. Despite being the traditional approach for water quality testing, the laboratory methods cannot give the real-time spatial overview that is necessary for the global assessment and monitoring of water quality [9]. In this study, by relying on the conventional water quality testing, the primary focus is on the analysis of the regression between the laboratory results and the results from the three imaging models, so as to determine their applicability in reservoir water quality estimation and prediction. For further analysis, a correlation of the distribution of the measured WQP using laboratory measurements and the three remote sensing models are spatially analyzed using Kriging.

In the use of remote sensing for the retrieval of water quality characteristics, the Landsat sensors, namely, multi-spectral scanner (MSS), thematic mapper (TM), enhanced thematic mapper (ETM+), and operational land imager (OLI) have been fairly used to estimate most of the important water quality parameters, such as chlorophyll-*a*, Secchi disk depth, total phosphorus, total suspended matter, turbidity, dissolved oxygen, biochemical oxygen demand, and chemical oxygen demand, as summarized in a review by [2]. Nonetheless, the use of Landsat data has the following limitations: (a) the repeat cycle of 16 days imposes major limitations on intraseasonal monitoring, especially in areas characterized by frequent cloud cover, and (b) the water quality parameter characteristics must be related to the inherent optical property (IOP) that can be measured by the satellite sensor [15].

By using Landsat data, several algorithms have been developed for the retrieval of WQP values from remotely sensed imagery. These algorithms are based on either

empirical models, semianalytical models, or matrix inversion models. The semianalytical models require both empirical and bio-optical data, and the above and in-water upwelling radiance, in order to describe relationships between water constituents and water surface reflectance. The matrix inversion models are based on a similar modelling scheme but also require prior knowledge of the water constituents, such as absorption coefficients or absorption slopes [16]. Because of the lack of these specific parameters, the matrix inversion models tend to be complex and impossible to calibrate. As such, empirical algorithms are more frequently used; however, with the following drawbacks, (i) they require a large sample size and (ii) they are very sensitive to local environmental conditions and, therefore, not applicable to other sites without additional field data. This means that the WQP estimation models and results obtained in specific geographic regions are not easily transferable to other case studies.

While there are extensive applications of remote sensing-based models to the case I waters, that is, open ocean waters, in-depth studies on inland freshwater bodies are complicated by the fact that remote sensing measurements of freshwater resources are far more complex, thus making it difficult to develop operational freshwater remote sensing algorithms. Secondly, it is not possible to use existing algorithmic models for accurate water quality estimation. Despite the algorithms having been validated in specific case studies, the localized characteristics of each area makes it necessary to reevaluate and revalidate the existing algorithms for their possible applications in other WQP prediction case studies.

To test the use of smartphones as fast, cost-effective, accurate, and simple to use techniques for WQP estimation, this study extends the use of remote sensing-based WQP retrieval to the utility of the EyeOnWater and HydroColor Smartphone sensor apps, which are designed to model and derive optically active water quality parameters. The apps operate on the principles of remote sensing reflectance and provide the potentially desirable low-cost and easy-to-use approach of monitoring the marine and or aquatic environments. While both smartphone apps use the RGB channels of the images acquired by the phone camera, they are based on different transfer functions in the colour space to estimate the water quality variables. Specifically, the EyeOnWater Colour app or water transparency is based on the Forel-Ule colour index (FUI) system and converts the RGB channels of the smartphone water surface image into the xyz chromaticity coordinates which is used to index the colour of the water in terms of the FUI. The HydroColor app on the other hand uses the same RGB channels of the smartphone taken of the reference gray card, sky, and water surface and converts this to the remote sensing reflectance  $R_{rs}$  (RGB). A summarized comparison between the EyeOnWater and HydroColor apps, including the advantages and disadvantages, is as presented in Table 1.

In this study, we showcase the results and usefulness of the smartphone apps in retrieving the apparent colour of water, Chl-*a*, turbidity, and SPM over a water reservoir, in comparison with the Landsat ETM+-VNIR reflectance data. The evaluation and validation of the results with laboratory experiments are carried out using empirical correlational

analysis, and in order to infer the distribution and variability of the measured water quality elements, Kriging is used to map and compare the spatial distributions of the selected WQP on the Kesses Dam, as a case study.

## 2. Literature Review

Water quality monitoring in freshwater bodies incorporating the use of sensor-based approaches, directly or indirectly, has become a major component in several water quality monitoring projects. As such, different studies have been conducted to establish the effectiveness of using remotely sensed water colour data in order to retrieve water quality variables. In the review by [2] on the water quality parameter estimations using remote sensing, it is observed that multispectral and hyperspectral data sources have been used to derive the biovolume concentrations, water turbidity, and suspended particulate matter content from various water bodies. In this section of the study, a review is presented on the use of remote sensing techniques in deriving water quality parameters, considering the utility of Landsat and the smartphone apps.

In order to develop and evaluate the relationships between hyperspectral remote sensing and lake water quality parameters chlorophyll, turbidity, and N and P species in a large manmade reservoir in Missouri (Mark Twain Lake), [18] analyzed the sampled data using a field spectrometer. From their study, it was concluded that the hyperspectral method was accurate in determining the turbidity and SPM in the reservoir, with strong correlations of  $R^2 \geq 0.7$ . Zhang et al. [19] also estimated the chlorophyll-*a* and SPM concentrations in a turbid lake (Taihu Lake, China) using 3-colour spectrophotometry and gravimetric methods. The results were sufficient and proved that the use of optical measurement techniques is more efficient than nonoptical measurement techniques, as the spectrophotometric method produced better results with  $R^2$  of 0.75. In determining the concentration of chlorophyll-*a* in reservoirs, [20] evaluated the performances of spectrophotometry, FluoroProbe, and high-pressure liquid chromatography (HPLC). The conclusion from the study was that spectroscopy was the more accurate method since it yielded higher and more realistic results.

In terms of using Landsat data, [21] estimated the chlorophyll-*a* concentration and tropic states of the Nalban Lake of East Kolkata, India, using Landsat OLI images and laboratory measurements. The prediction model developed by applying regression analysis between the band ratios yielded  $R^2$  of 0.78. Zheng et al. [22] presented a long-term multitemporal Landsat-based monitoring of total suspended matter concentration pattern change in the wet season for Lake Dongting in China to determine the SPM variations. Based on the in situ measurements, an algorithm was developed based on the near-infrared (NIR) band to estimate total suspended matter (TSM) distribution. The study showed a sufficient correlation between NIR band reflectance values and TSM estimates from the field measurements. And to estimate the total suspended solids and chlorophyll-*a*, [23] developed Landsat OLI-based water quality parameter retrieval algorithms and

TABLE 1: Comparisons between EyeOnWater and HydroColor apps [17].

EyeOnWater	HydroColor
(a) <i>Required image(s)</i> Water surface image	Gray card, sky, and water surface images
(b) <i>Reference material</i> Digitalized FU colour comparator scale as reference material. The user can add information on modern FU scale and Secchi disc measurements	No reference material is required
(c) <i>RGB transfer function</i> From sRGB of water surface image to xyz chromaticity coordinates	From sRGB of gray card, sky, and water surface images to RGB
(d) <i>Colour space conditions</i> XYZ colour space; not dependent on the device used. Also, the resulting chromaticity coordinates do not depend on the illumination condition of which the image was taken	RGB colour space; dependent on the device used. This is because it is influenced by the specific spectral response function of the capturing device. Also, it depends on the illumination condition of which the image was taken
(e) <i>Estimated water quality variables</i> Water surface colour translated to FUI	Water turbidity (0–80 NTU), SPM ( $\text{g}/\text{m}^3$ ), and backscattering coefficient in the red ( $\text{m}^{-1}$ )
(f) <i>Advantages</i> It is only the upwelling light from the water surface that carries any useful information on the water body. By this, it only requires an image of the water surface which would be easier for citizen monitoring	In deriving the RGB using the three images, error incurred from each image as a result of the smartphone cancels out. Thus, the phone camera needs no calibration
(g) <i>Disadvantages</i> The weather conditions of the location are given as parameter values to be selected by the user concerning the location and not of the pertaining condition of the location. This can result in an optimistic estimate of water quality variables without correcting sun-sky glint effects on the water surface image	Does not take into account the weather conditions such as the wind which can affect the resulting output. It is cumbersome for citizens who would like to take random measurements without the availability of a gray card

correlated the results for nine (9) stations with laboratory experiments. The results showed that the regression model for estimating TSS produced high accuracy with a coefficient of determination of  $R^2$ , normalized mean absolute error (NMAE), and root mean square error (RMSE) of 0.709, 9.67%, and  $1.705 \text{ g}\cdot\text{m}^{-3}$ , respectively, while that for chlorophyll-*a* produced  $R^2$  of 0.579, NMAE of 10.40%, and RMSE of  $51.946 \text{ mg}\cdot\text{m}^{-3}$ .

Further, [24] established a relationship between laboratory-derived water quality data and the pixel reflectance values from Landsat ETM satellite data for the estimation of chlorophyll-*a*, suspended solid matter, Secchi disk, and total phosphate maps for the Ömerli Dam with sufficient accuracy. Torbick and Corbiere [25] carried out a multiscale-based mapping assessment of Lake Champlain for chlorophyll-*a* and phycocyanin retrieval, and by using empirical band ratio regressions, they determined the Chl-*a* concentrations with  $R^2$  and RMSE ranging from 0.76–0.88 and 0.42–1.51, respectively. Waxter [26] used in situ measurements from the Tenmile Lakes Basin to calibrate reflectance values from the Landsat TM. The results showed a good linear correlation between turbidity and radiance, which were inversely related in algal dominated areas. In another study, [27] summarized the previous studies on the use of Landsat TM/ETM+ for Chl-*a* determination and estimated the chlorophyll concentration in a freshwater Lake Jordan using

Landsat OLI imagery. They examined the relationship between the reflectance value of an individual OLI band and the in situ Chl-*a* concentration in order to identify the bands sensitive to chlorophyll-*a*. By developing two optical band-based linear equations, the relationship between the ratio-based spectral index and Chl-*a* concentration from different stations was derived, and the spatial distribution of Chl-*a* was also mapped. They reported a significant correlation between the spectral index from Landsat OLI imagery and Chl-*a* in Jordan Lake, for different months of the year. Further, [28] recently used the SmartFluo app, which is based on stimulated fluorescence of water constituents, to measure the fluorescence of chlorophyll-*a*. In comparison with the laboratory experiments, SmartFluo showed a linear correlation of  $R^2 = 0.98$  to the chlorophyll-*a* concentrations as measured using a benchtop laboratory fluorometer (LS 55, PerkinElmer).

Na et al. [29] estimated and mapped the water turbidity based on Landsat imagery for Lake Paldang, Korea. Based on the field measurements and the principal component analysis (PCA), the PC bands were found to be suitable in estimating the turbidity, with  $R^2$  of 0.6319 on regression with the in situ data. The study emphasized on the necessity to monitor continuously the in situ data as well as the reflectance features so as to accurately determine the environmental factors of water quality. Olet [30] examined the

correlation in water quality in Roxo reservoir using Landsat images and in situ measurements, for chlorophyll-*a* and SPM measurements. An image-based correction was implemented using in situ water leaving reflectance (WLR) and a model developed to estimate the two WQP, whereby SPM was inferred from the chlorophyll-*a* model. Chlorophyll-*a* was derived with  $R^2$  of 0.295 and RMSE of  $0.603 \mu\text{g}\cdot\text{L}^{-1}$ , while SPM concentration ranged from  $9 \text{ mg}\cdot\text{m}^{-3}$  to  $34 \text{ mg}\cdot\text{m}^{-3}$  with an  $R^2 = 0.5$  and  $\text{RMSE} = 0.145 \text{ mg}\cdot\text{m}^{-3}$ .

From the literature review, it is evident that several studies continue to be conducted in order to develop algorithms or models for monitoring water quality in different types of inland water bodies, especially lakes, from Landsat MSS, TM, ETM+, and OLI sensor data. Other satellite data have also been used including SPOT HVR, MODIS, NOAA-AVHRR, MERIS, IRS-1C, Hyperion, IKONOS, and Quick-Bird, as summarized in [31]. This observed increase in the use of remote sensing techniques for extracting water quality information is because of the effectiveness of remote sensing than the direct field measurements in terms of cost, speed, and spatial-temporal coverage.

The EyeOnWater (<http://eyeonwater.org>), which is based on the EU-FP7 project CITCLOPS, is a system developed for the retrieval and use of data on natural-water colour, transparency, and fluorescence, by using low-cost sensors combined with contextual information, in order to estimate the optically active water constituents. With the EyeOnWater app, it is envisaged that water managers and consumers can be able to acquire water quality data by imaging the water surface, and through online mobile application interface, the water quality parameters can be obtained. In using EyeOnWater for water quality assessment, [17], in comparison with the HydroColor app, estimated the retrieval of turbidity, SPM, colour, and chlorophyll for a case study of three lakes in the Netherlands. The study showed that the correlation of smartphone images and the RAMSES hyperspectral radiometer was accurate with  $R^2 = 0.65$ . The study recommended the use of EyeOnWater as an easy and efficient application for water quality monitoring, for the case study of the lakes in the Netherlands. Busch et al. [32, 33] also compared ocean colour satellite measurements with the EyeOnWater app local colour observations, with in situ laboratory and field tests in the determination of the water colour, transparency, chlorophyll-*a* fluorescence, and phytoplankton dynamics, respectively. Their results showed accuracies of more than 90% and also demonstrated the effectiveness of colour-based low-cost sensors for citizen-based contributions in filling observational gaps and increasing environmental stewardship among the public in monitoring their environments [28, 32, 34].

In testing the validity of EyeOnWater, two case studies in Spain and Germany were used to investigate on the retrieval of water colour, turbidity, SPM, and chlorophyll. By digitizing the colours of the Forel-Ule scale to establish the colour of natural waters through smartphone imaging by the use of high-quality-illumination filters and a frame made of white Plexiglas, the creation of a colour comparison tool for recording not only the colour in terms of the FU system but also the chlorophyll concentration, turbidity, and

suspended particulate materials was developed. Wernand et al. [7] used the FU datasets, which forms the basis of EyeOnWater colour-based water quality assessment, to estimate the global changes occurring in the ocean in relation to the Chl-*a*, CDOM, and SPM concentrations, for the case study of the Dutch Wadden Sea conservation area.

Bardaji and Piera [35] presented a review on the first crowdsourcing technologies to estimate water transparency based on a sensor attached to low-cost moorings attached to buoys, which integrated different modules such as light sensors, microprocessors, and communication modules for the measurement of water colour, transparency, and fluorescence. The review led to adoption of quasidigital optical sensors which convert light (irradiance) measurements into a frequency signal. With the simple conversion, it is possible to directly estimate the light intensity without the need of analog-to-digital-converter devices in determining water quality parameters.

For water colour monitoring, [36] introduced the FUME algorithm that converts the MERIS satellite reflection data to FU scale by transforming a number of MERIS images into the FU colour scale images and comparing the in situ observed FU numbers, with the modelled FU numbers from in situ radiometric measurements. The FUME algorithm converts the normalized water leaving reflectance from nine MERIS bands into a discrete FU number to monitor water colour. In a related study, [37] estimated SPM by derivation of a single band algorithm by parameterizing Gordon's approximation of the irradiative transfer model with measurements of inherent optical properties. This led to development of the POWERS algorithm for estimating near-surface SPM concentrations. Davies-Colley and Smith [38] used the Compact Airborne Spectrographic Imager (CASI) hyperspectral imagery for water colour mapping and established a colour matching function as a simple standard way to monitor the colour of aquatic systems. It was established that the standard RGB values are converted to the XYZ CIE colour system using the conversion matrices found in [39]. In summary, it is evident that previous studies have contributed to the development of alternative tools for analyzing water quality parameters in order to supplement laboratory measurements. Notably, however, most studies have not applied the smartphone apps in the comprehensive assessment of water quality parameters, with the objective of retrieving and assessing the water colour, Chl-*a*, turbidity, and SPM of productive inland water bodies like reservoirs and/or lakes.

The HydroColor smartphone app [40] was built with the objective of crowdsourcing water quality data. The iPhone-based app uses three images—gray card, water, and sky images [41]—to derive the reflectance of natural water bodies. From the reflectance values, the app automatically generates the turbidity and SPM levels in the water; however, the colour and chlorophyll parameters have to be computed using a suitable conversion algorithm. Objectively, by aggregating data from the public over large spatial and temporal scales, the HydroColor app can determine the typical turbidity or chlorophyll values for different environments. The interactive online database can then be used by experts or the general public to help monitor for changes, such as

increased occurrence of algal blooms or erosion leading to higher suspended sediment.

Whiting [42] used the HydroColor app to retrieve the turbidity in the Union River. With TSS of  $13 \text{ mg}\cdot\text{L}^{-1}$ , turbidity of 6.5 NTU, and  $R^2$  of 0.7183, the study concluded that HydroColor was suitable for estimating and predicting the turbidity and TSM. In the use of sensor-based models in studying turbid waters in Barga (Netherlands), [43] used the HydroColor app to detect fluctuations in water changes. The study recorded  $R^2$  of 0.547 and RMSE = 4.7 NTU, and the app was also recommended as suitable for the measurement of turbidity and SPM; however, the results were influenced by cloud cover and sample size, as was also observed by [29]. In a comparative study, [44] compared the utility of the iOcean RGB sensor and HydroColor apps for turbidity and water colour monitoring. While a correlation was impossible in colour measurements as HydroColor gave discrete data on colour, a logarithmic correlation with  $R^2$  of 0.68 was achieved using the HydroColor app. Mahama [17] carried out a comparative assessment on the utility of HydroColor and EyeOnWater apps for the measurement of turbidity, SPM, colour, and chlorophyll in comparison with laboratory measurements and hyperspectral imagery. The results, respectively, showed that from the EyeOnWater and HydroColor apps, the SPM was estimated with  $R^2$  values of 0.79 and 0.90, while turbidity was determined with correlation coefficients  $R^2$  of 0.73 and 0.63. For a comparative evaluation, the HydroColor app is tested for the estimation of water quality parameters at the spatial scale of a reservoir and in comparison with the Landsat ETM+ and the EyeOnWater app.

From the literature review, it is evident that several models have been used to retrieve water quality from remote sensing data. The models, as already been stated, comprise of empirical, semiempirical, and analytical models, which have been applied in order to estimate and produce quantitative water quality maps using different sensors [45]. The most often used empirical models are based on the development of bivariate and or multiple regressions between the sensor data and measured water quality parameters, whereby the digital numbers or radiance values at the sensor as well as their band combinations are correlated with the laboratory measurements of water quality parameters usually collected in coincidence of the sensor time of acquisition or overpass [46]. The semiempirical approaches are often used when the spectral characteristics of the parameters of interest are known. The spectral characteristics are then included in the statistical analysis by focusing on well-chosen spectral areas and appropriate wavebands used as correlates [47]. In the analytical modelling, the water quality parameters are related to the inherent optical properties by using specific inherent optical properties (SIOPs). The IOPs of the water column are then related to the apparent optical properties (AOPs) and hence to the top of atmosphere (TOA) radiance, such as that described by the radiative transfer theory [48, 49].

Despite the need for integrated assessment of water quality variables in determining the health of water bodies, most studies have focused on the retrieval of a single water quality parameter and for specific case studies. Since relationships

between reflectance and water quality will vary across ecoregions, reservoir taxonomy, and seasons which are impacted by local environmental conditions including weather events, it is difficult to develop universal predictive models to extract water quality parameters from remote sensing data. For that reason, these relationships must be developed independently for each region of interest. Further, due to the subjectivity of previous studies to specific ecoregions and water quality parameters, the current study develops an empirical approach for retrieving remotely sensed reflectance values from Landsat ETM+-VNIR imagery based on water sample point locations for water quality monitoring of Kesses Dam in Kenya.

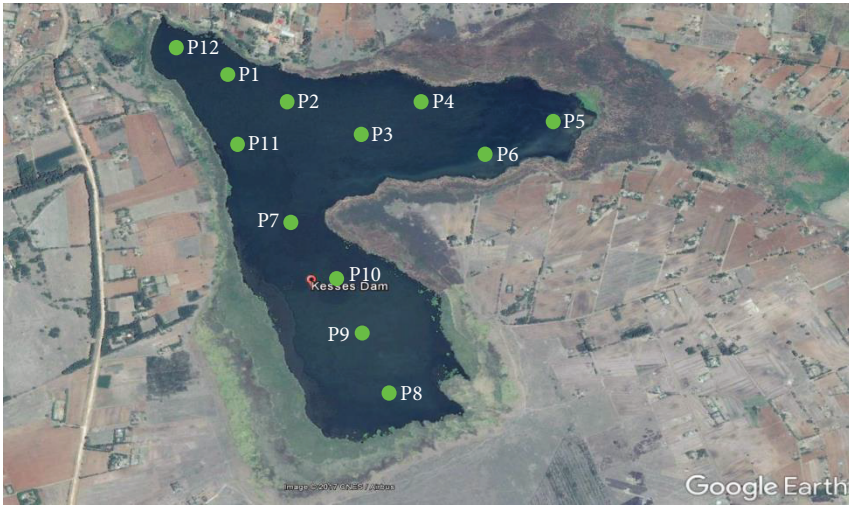
### 3. Methodology

*3.1. Case Study and Sampling.* As already mentioned, the case study for the comparative evaluation of the three sensor-based models is Kesses Dam in Uasin Gishu County, Kenya. The reservoir, located at longitude  $35^{\circ}20' \text{ E}$  and latitude  $0^{\circ}16' \text{ N}$ , is fed by two inlet rivers and one outlet river (Table 2). Built in 1958, the dam is one of the 75 small reservoirs within the county. With an initial capacity of approximately 2.4 million cubic meters, the volume has reduced to about 1.8 million. The dam is the main drinking water source for the surrounding community including Moi University and the growing neighbouring urban and rural populations [50]. Over the years, the use of the reservoir's water has diversified to include domestic drinking, irrigation, recreation, and fishing. Despite the significance and overdependence on the dam's water, there is hardly any monitoring carried out on its water quality.

Waters drained from the agricultural areas are the main source of pollution within the watershed, and there is eminent presence of algal blooms which may be a reflection of increased nutrient transport within the basin. Additionally, domestic sewage and soil erosion have resulted into increased turbidity and siltation of the reservoir and to the overall loss of water quality in the water body. Nonetheless, monitoring public waters can be complicated due to the fact that field sampling campaigns are labor- and time-intensive and often require additional laboratory costs for sample analysis. To monitor such dams, remote sensing models, especially the smartphone-based models, can be cost-effectively employed in the field for public or crowdsourcing of dam water quality.

To monitor the water quality in the case study dam, twelve (12) evenly distributed and coordinated water quality sampling stations were set up within Kesses Dam, as illustrated in Table 2. Water samples were collected at 0.45 m depths, in order to determine concentrations of Chl-*a* and SPM, turbidity, and water colour following the standard laboratory protocols. The timing of the field campaign for in situ sampling and the Landsat satellite overpass schedule were prefixed, such that the sampling was carried out on the 26th of March 2017, which was concurrent with the date of imagery acquisition from Landsat ETM+. As reported in [51], synchronization of the sampling and the satellite image acquisition to within  $\pm 1$  day of the satellite image is recommended for best calibration results. The dry season period

TABLE 2: Google map-based location of the case study of Kesses Dam and the coordinates of the sampling stations.

Case study dam and the sampling stations (P)	Location coordinates of the sampling stations		
	Station ID (Pi)	Easting (m)	Northing (m)
	P1	759505.00	31612.00
	P2	759740.00	31468.00
	P3	760000.00	31415.00
	P4	760271.00	31427.00
	P5	760582.00	31427.00
	P6	760412.00	31290.00
	P7	759804.00	31236.00
	P8	760183.00	30252.00
	P9	760123.00	30486.00
	P10	759852.00	30578.00
	P11	759479.00	31447.00
	P12	759323.00	31681.00

was chosen because during this time the composition of reservoir water is relatively stable, and the images are cloud-free. To reduce the errors in sample site locations, and to correlate the reflectance and water quality parameters, an average spectral reflectance of  $2 \times 2$  pixels neighbourhood configuration was used as suggested by [52]. The neighbourhood-based analysis also minimizes the probable errors in GPS measurements during sampling.

### 3.2. Retrieval of Water Quality Parameters

#### 3.2.1. Landsat ETM+-VNIR Data.

(1) *Radiance and Reflectance Determination.* The Landsat ETM+ is a near polar-orbiting sun-synchronous satellite, with a 16-day repeat cycle, at an altitude of 705 km altitude and swath-width of 185 km. Its payload is the ETM+ sensor, which is a single nadir-pointing instrument, and provides for an eight-band multispectral scanning radiometer which detects spectrally filtered radiation in VNIR, SWIR, LWIR, and panchromatic bands. From the literature review, it was inferred that Landsat TM and ETM+ have been widely used for water quality parameter derivation, due to their wider and hence spectrally appropriate resolutions as compared to other sensors [2, 53, 54].

In this study, only the VNIR ETM+ bands were used for analysis and detection of the optically active water quality parameters. This is because the long-wave bands provide little or no information for water quality assessment [55–57]. The VNIR are in the spectral range where light passing through the water body provides some information about the optically active water constituents [58]. As depicted in Figure 1(a), a comparison of the spectral resolutions of Landsat ETM+/TM with the Landsat OLI shows that in VNIR, ETM+ has higher spectral resolution, implying that it can detect the more optically active particles in water than the OLI sensor. Further, in Figure 1(b), a comparison of the

spectral resolutions of ASTER, OLI, ETM+, and Sentinel-2A shows that the spectral resolution of ETM+, which is similar to that of the TM sensor, is wider and more suitable for the detection of WQP [2, 8, 59].

The estimation of water quality parameters from satellite images is dependent on the accuracy of atmospheric correction and water quality parameter retrieval algorithms. However, most of previous studies as summarized in [46, 60] either correlate the Landsat bands to the raw digital numbers, radiance, spectral radiance, or reflectance, with or without atmospheric correction of the data. This limits the possibilities of finding a clue to a physically sound analysis, and most of the algorithms proposed are only applicable to the one single scene that has been investigated. By using the FLAASH model, the Landsat ETM+-VNIR imagery is atmospherically corrected [53, 60–62], whereby the digital numbers are first converted to the spectral radiance units according to (1).

$$L_{\lambda} = M_{\rho} * QCAL + A_{\rho} \quad (1)$$

Equation (1) can also be rewritten in terms of Eq. (2), whereby the DN values are used to obtain the at sensor radiance or top of atmosphere (TOA) reflectance  $L_{\lambda}$ .

$$L_{\lambda} = \left\{ \frac{L_{\max_{\lambda}} - L_{\min_{\lambda}}}{QCAL_{\max}} \right\} * QCAL + L_{\min_{\lambda}}, \quad (2)$$

where  $L_{\lambda}$  is the spectral radiance at the sensor's aperture at TOA ( $Wm^{-2}Sr^{-1}\mu m^{-1}$ ),  $M_{\rho}$  is the multiplicative scaling factor or the data product "gain" in  $Wm^{-2}Sr^{-1}\mu m^{-1}/DN$ ,  $A_{\rho}$  is the rescaled bias or the data product "offset" in  $Wm^{-2}Sr^{-1}\mu m^{-1}$ ,  $L_{\min_{\lambda}}$  is the spectral radiance scaled to  $QCAL_{\min}$  ( $Wm^{-2}Sr^{-1}\mu m^{-1}$ ),  $L_{\max_{\lambda}}$  is the spectral radiance scaled to  $QCAL_{\max}$  ( $Wm^{-2}Sr^{-1}\mu m^{-1}$ ),  $QCAL_{\max}$  is the maximum DN (255), and QCAL is the quantized calibrated pixel values in DN, specific to a sample site point.

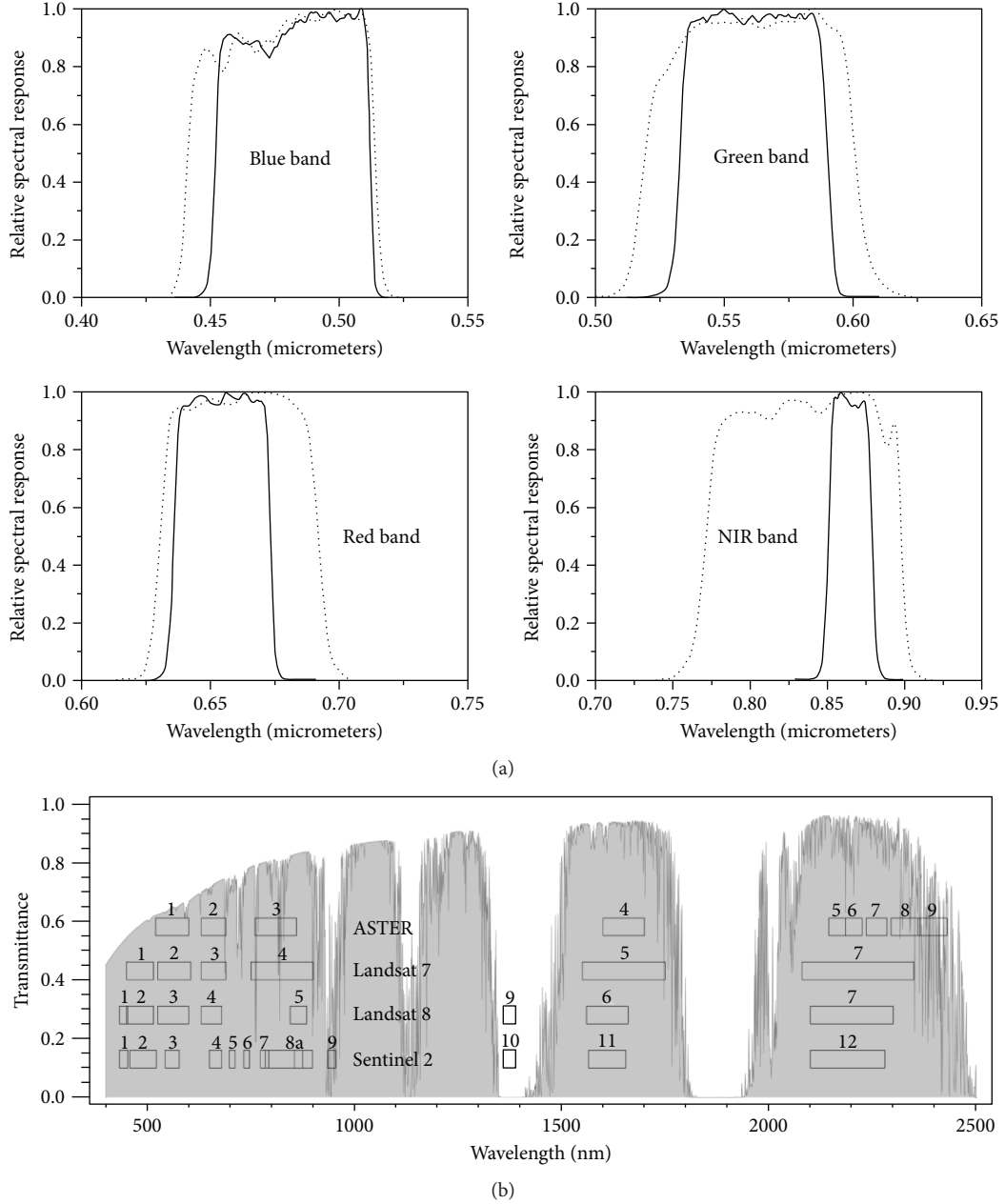


FIGURE 1: (a) Relative spectral responses of the spectral band differences between Landsat ETM+ (dotted curve) and Landsat OLI (solid curve). (b) Comparisons of spectral resolutions of ASTER, TM, ETM+, and Sentinel-2A sensors. [http://landsat.usgs.gov/tools\\_spectralViewer.php](http://landsat.usgs.gov/tools_spectralViewer.php).

While in (1) and (2) the DN is converted to the TOA reflectance, this does not account for or minimize the atmospheric effects. The haze effect is one of the most important atmospheric effect parameters due to the scattering and absorption of the radiation by molecules and aerosols [62]. Techniques for haze removal can be categorized into (i) simple dark object subtraction (DOS) method and (ii) atmospheric transmission model in combination with in situ field measurements. By calculating the rescaling factors from the minimum and maximum calibration values, the DOS and sun angle corrections are applied by expanding (1) and (2), to (3), (4), and (5) as in [60].

$$L_{\text{haze}} = HL_{\min} - L_{1\%}, \quad (3)$$

where

$$HL_{\min} = L_{\min} + DN_{\min} \frac{(L_{\max} - L_{\min})}{(QCAL_{\max} - QCAL_{\min})}, \quad (4)$$

$$L_{1\%} = \frac{0.01 + ESUN_{\lambda} * \cos((90 - \theta_s)\pi/180)^2}{d^2 \pi}. \quad (5)$$

$L_{\min}$  and  $L_{\max}$  are, respectively, the minimum and maximum spectral radiance values scaled to  $QCAL_{\min}$  and



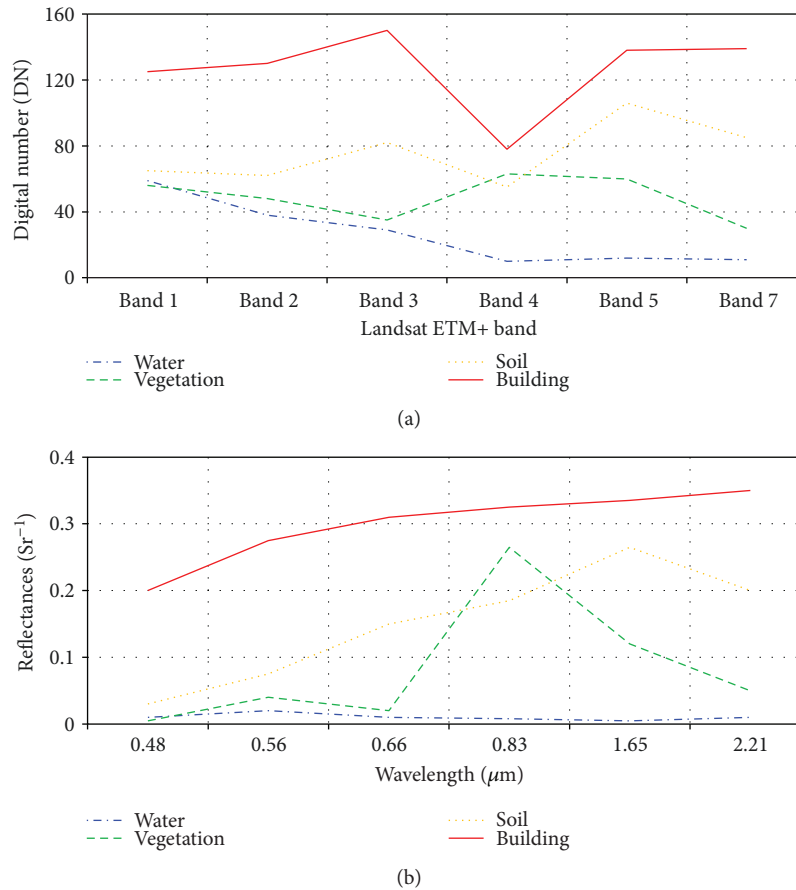


FIGURE 2: DN and reflectance curves of four target surface features, before (a) and after (b) atmospheric correction.

$QCAL_{max}$  by band, and for 8-bit imagery, the difference between  $QCAL_{min}$  and  $QCAL_{max}$  is 254;  $DN_{min}$  is the least pixel value as converted to TOA reflectance  $HL_{min}$ ;  $ESUN_{\lambda}$  is the solar spectral irradiance at TOA;  $\theta_s = 90 - \theta_s$  is the solar zenith angle in degrees ( $90^\circ$  sun elevation) and is calculated from the sun elevation included in the metadata; and  $d$  is the Earth-sun normalized with respect to mean of 1.0 AU.

The satellite data should be made to be comparable with the in situ spectral measurements by converting from radiance to at-satellite reflectance, also called the remote sensing reflectance  $R_{rs} = \rho_{\lambda}$ . The outcome  $L_{haze}$  is then the rescaled and corrected  $DN_{min}$  value used to correct the rescaled image values during their correction process according to (6), where  $P_{\lambda}$  or  $R_{rs}$  is the unitless atmospherically corrected reflectance, and is the final outcome of the difference between TOA reflectance  $L_{\lambda}$  and the rescaled and corrected  $DN_{min}$ . Equation (6) can also be rewritten in terms of the TOA reflectance  $R_{rs}(\lambda)$  as shown in (7).

$$P_{\lambda} = \frac{\pi(L_{\lambda} - L_{haze})d^2}{ESUN_{\lambda} \cos(\pi/180\theta_s)}, \quad (6)$$

$$R_{rs} = \frac{\pi * L'_{\lambda} * d^2}{EUS_{\lambda} * \cos \theta_s}. \quad (7)$$

Figure 2 presents a comparison of four target features before and after atmospheric correction of the multispectral

bands. As compared to other natural features like soil and vegetation, the fraction of light reflected from water is observed to be very low [63] and is only significant in the VNIR bands [8]. This means that the determination of the accurate and absolute radiometric correction of the sensor is critical [64]. From the results in Figure 2, it is observed that the DN curves of the test features are similar to the corresponding curves of the same features after atmospheric correction, in terms of the spectral reflectance.

(2) *Correlating Landsat ETM+-VNIR Bands and Water Quality Parameters.* As already stated, there are primarily three categories of regression algorithms, namely, empirical algorithms, theoretic algorithms, and their combinations, which can be used in modelling and extraction of water quality indicators from remote sensing data. Bivariate and multiple regression techniques have been used in different studies to come up with the relating equation models for WQP estimations [53]. To determine the suitable models in terms of correlation, stepwise bivariate linear regressions were used. This study used the empirical algorithms to establish the bivariate correlations between the Landsat ETM+-VNIR band reflectances and the in situ water quality variables. The following remote sensing independent reflectance bands and band combinations as presented in Table 3 were considered for the statistical analysis of the Landsat data in the estimation of the

TABLE 3: Summary of Landsat ETM+-band combinations for water quality determination.

Landsat ETM+-VNIR bands and combinations	
(i) Single ETM+-VNIR bands	B1, B2, TM3, and B4
	B1 and B2; B1 and B3
	B1 and B4; B2 and B3
	B2 and B4; B3 and B4
(ii) Linear band combination	B1, B2, and B3
	B1, B2, and B4
	B2, B3, and B4
	B1, B2, B3, and B4
(iii) VNIR band ratios	B2/B1; B1/B3; B3/B1; B4/B3; B4/B1; B3/B2; B4/B2
	(B1/B3) + B1 (B1/B4) + B1
(iv) Mixed NVIR band combinations	(B1/B4) + B2 (B1/B3) + B2 (B1/B3) + B3 (B4/B1) + B4

water quality parameters, using the empirical mathematical models.

The single bands, band ratios, and combinations of the bands, as presented in Table 3, were used in the regression analysis. In the optimization of the regression analysis results, the appropriate regression method is selected based on the results with a high  $R^2$  value, between the predicted model and the laboratory-measured WQP [57]. The fit of the model was tested at the entry significance level  $p$  of 0.05 and the removal significance at a level of 0.10. Finally, the  $t$  test at the confidence level of 95% was then used to accept the determined regressive model.

The empirical models used in the regression of the in situ measurements to the Landsat bands comprised of the following generalized equations, where WQP is the water quality parameter,  $R_{rs}(\lambda)$  is the reflectance at the VNIR band, and  $A$ ,  $B$ , and  $C$  are the model constants.

(a) Linear:  $A * R_{rs}(\lambda) + B$

(b) Polynomial:  $A * R_{rs}(\lambda)^2 + B * R_{rs}(\lambda) + C$

(c) Logarithmic:  $A * \log_{10} R_{rs}(\lambda) + B$

(d) Power:  $A * R_{rs}^B(\lambda)$

(e) Exponential:  $Ae^{B * R_{rs}(\lambda)}$

To compare the algorithmic results from the current study with prior case study results, the results from the empirical models based on the band combinations and regression analysis were compared with those from the following related WQP estimation algorithms, as expressed in (8), (9), and (10), respectively, for Chl- $a$ , SPM, and turbidity. The chosen algorithms are for comparisons and are on the basis of the same type of water body and also with reasonable water quality parameter estimation results. Because they are

developed for different environmental and climatic conditions and factors, the equations are only used as indicators, and scene-specific algorithms are developed.

- (a) Chl- $a$  and SPM estimation using the [23] algorithm

$$\text{Chl-}a = 4180.5 \left( \frac{\log R_{rs_2}}{\log R_{rs_4}} \right) - 6211.4 \left( \frac{\log R_{rs_2}}{\log R_{rs_4}} \right) + 2540.2, \quad (8)$$

$$\text{SPM} = 32.42 \left( \frac{\log R_{rs_2}}{\log R_{rs_4}} \right) - 12.719, \quad (9)$$

where  $R_{rs_2}$  and  $R_{rs_4}$  are the calculated reflectance at the various sampling stations for Landsat ETM+ bands 2 and 4.

- (b) Turbidity prediction using the Waxter [26] algorithm

$$\text{Turbidity} = -0.0016B_1^2 + 0.2504B_1 - 1.0014 \quad (10)$$

where  $B_1$  is the DN of Landsat ETM+ band 1.

3.2.2. *EyeOnWater App*. (1) *WQP Derivation from EyeOnWater App*. EyeOnWater, initially referred to as CITCLOPS, is a low-cost and easy-to-use smartphone application tool, developed for monitoring the quality of natural water bodies. The app utilizes the FUI colour system. This means that in the EyeOnWater system, the estimated water quality variable is the water colour which is translated into FUI for WQP analysis. The following steps summarize the approach for EyeOnWater as detailed in [65, 66]. In order to automate the process of converting the FU values to the actual WQP estimates online, an extension app to the EyeOnWater app—called the FU converter—was developed in this study, for the conversion and computation of the user-determined FU values.

- (i) Acquisition of standard RGB (sRGB) images using an Android operating system (OS) smartphone camera
- (ii) Gamma expansion: carried out on the specular reflection at water-air interface to return each band's DN to the linear level [67]
- (iii) Conversion of sRGB image to the equivalent tristimulus values in XYZ colour space using the Pascale [68] conversion matrix  $M$
- (iv) Water illumination correction: to cater for the variation in illumination caused by time of observation, local water weather condition, and water surface roughness, the illuminations are standardized using the cone response matrix [39].
- (v) Conversion of XYZ tristimulus values to the  $(x, y)$  chromaticity coordinates and the relation to the FUI values, where  $x = X/(X + Y + Z)$  and

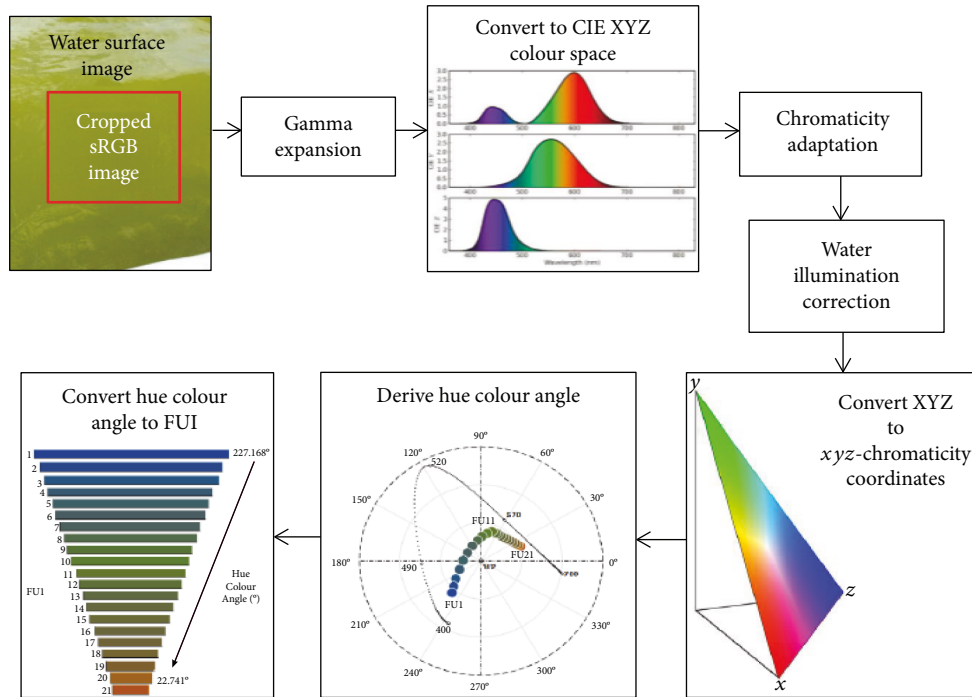


FIGURE 3: Diagrammatic flowchart for water image processing using EyeOnWater app [6].

$y = Y/(X + Y + Z)$  defines the  $(x, y)$  chromaticity coordinates

- (vi) Conversion of the  $(x, y)$  chromaticity coordinates to the corresponding chromaticity angles or water angle:  $\alpha_w = \arctan(y_i - y_w, x_i - x_w)$  modulus  $2\pi$ , where  $(y_i - y_w)$  and  $(x_i - x_w)$  are the chromaticity coordinates derived from the image  $i$  with respect to the origin or white point  $w$  [65]
- (vii) Selection of the best subimage using the percentile rule, which then reveals the true colour of the water body at the time of exposure
- (viii) Using the FUME algorithm as in Wernand et al. [7] to convert the chromaticity angle of the subset image to FU index
- (ix) Transformation of the FU index into turbidity and SPM water quality parameters using the [40] correlation functions
- (x) FU analyzer and convertor web application: design and extend a new app to convert FU values obtained from the EyeOnWater app as entered by a user, to readily understandable water quality parameters which include turbidity, chlorophyll, SPM, and the corresponding water colour and significance

Figure 3 presents a structural diagram of the above outlined processes as used to derive the  $xyz$  chromaticity coordinates, hue colour angle  $\alpha_w$ , and FUI from the smartphone images.

The proposed FU analyzer and convertor program consists of the user interface (front-end) and processing logic

(back-end component). The input into the MySQL database server consists of the FU values and the corresponding chromaticity angles and the water colour values with the corresponding significances. From the input, an asynchronous Ajax request is made to the PHP script that processes the data and returns results instantaneously. For the FU conversion application, the following algorithms proposed by [40] were used for the online estimation of turbidity, Chl- $a$ , and SPM.

$$\text{Turbidity} = \frac{22.57 * \alpha_w(R)}{5.87 - \alpha_w(R)}, \quad (11)$$

$$\text{Chl-}a = 0.061 * e^{-0.666 \cdot \text{FUI}}, \quad (12)$$

$$\log_{10} \text{SPM} = 1.02 * \log_{10} \text{turbidity} - 0.04. \quad (13)$$

The prototype for the extended online EyeOnWater FUI analyzer and convertor is presented in Figure 4, where the first screenshot (Figure 4(a)) is the analyzer and the second is the convertor (Figure 4(b)).

(2) *Validation of  $x$ -Chromaticity Coordinates.* As a validation step, the relationship between the  $x$ -chromaticity coordinate and laboratory-measured turbidity and SPM are first evaluated. As shown in Figure 5, a 5-degree polynomial correlation fit of the measured turbidity and  $x$ -chromaticity gave an RMSE of 4.89053 NTU and  $R^2$  of 0.5659, while the SPM correlation gave an RMSE of 5.8724  $\text{mg} \cdot \text{m}^{-3}$  and  $R^2$  of 0.7175. These validation results show that it is viable to quantify the water quality variables from the  $xyz$  chromaticity coordinates. The results also imply that the app's FUI can be effectively related to the optical water quality variables.

In order to compare the user-observed water surface images with the calculated FU results from EyeOnWater

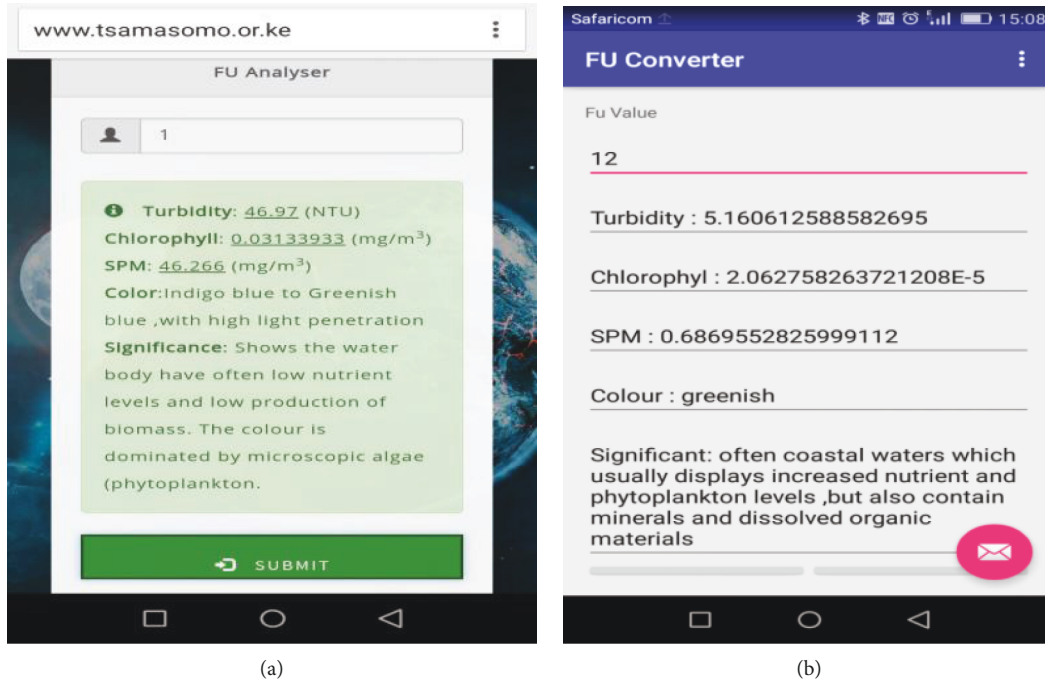


FIGURE 4: Screenshot showing the display of WQP from the Android APK web application and FUI analyzer.

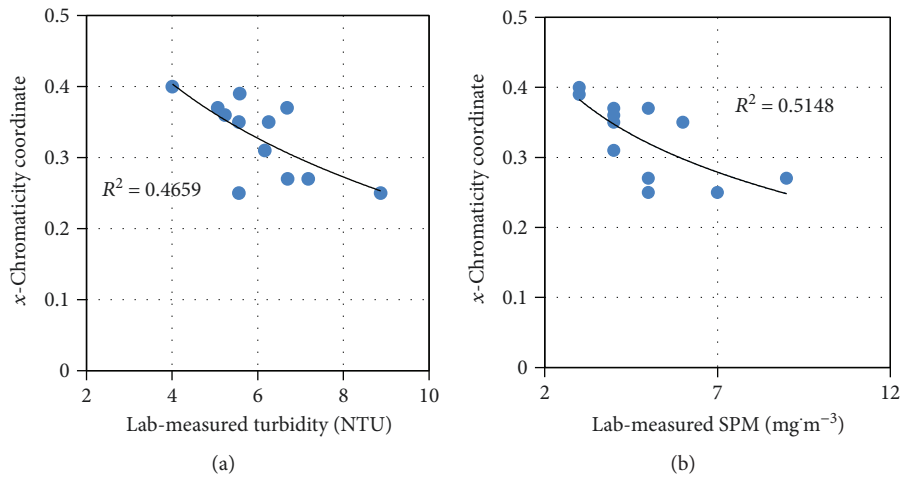


FIGURE 5: Relationship between laboratory-measured turbidity and SPM, with the  $x$ -chromaticity coordinate from the EyeOnWater app as a validation step.

app results, a correlational analysis was carried out such that the water surface images were matched with the FU scale as proposed in [36]. The results in Figure 6 indicate a good correlation of a linear fit with a coefficient of determination of  $R^2 = 0.645$  and RMSE of 1.607. The validation results in Figures 5 and 6 show that the EyeOnWater app is suited for field measurements.

**3.2.3. HydroColor App for Water Quality Data Estimation.** In using the HydroColor app, an iPhone OS camera is used to acquire three images comprising of gray card, sky, and water surfaces, so as to obtain the sRGB colours. The iPhone camera is a traditional CMOS array covered by a Bayer filter, and the filter provides three spectrally

wide-red, green, and blue colour channels. Using the three images, the app calculates the remote sensing reflectance in the red, green, and blue (RGB) colour channels of the camera. Figure 7 shows sample images taken by an iPhone camera on a clear day (Figure 7(a)) and on a cloudy day (Figure 7(b)) from the same sampling point [40]. The images in Figure 7 show that the environmental conditions such as cloud cover and sunlight intensity will influence the quality of the water colour.

A sample water image from the data analysis page of the HydroColor app is clipped and uploaded to the colour PhytoBlog for water quality determination as depicted in Figure 8. In minimizing the surface reflection of skylight in the water image, HydroColor contains a sun model that uses

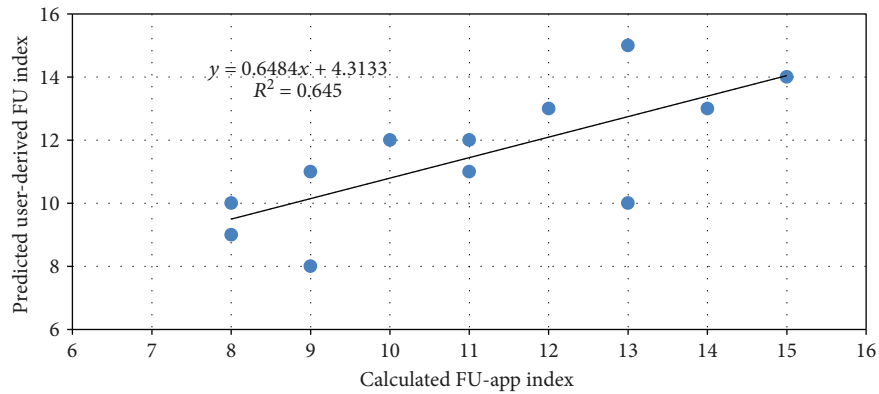


FIGURE 6: Calibration between calculated FU-app and predicted FU-user values.

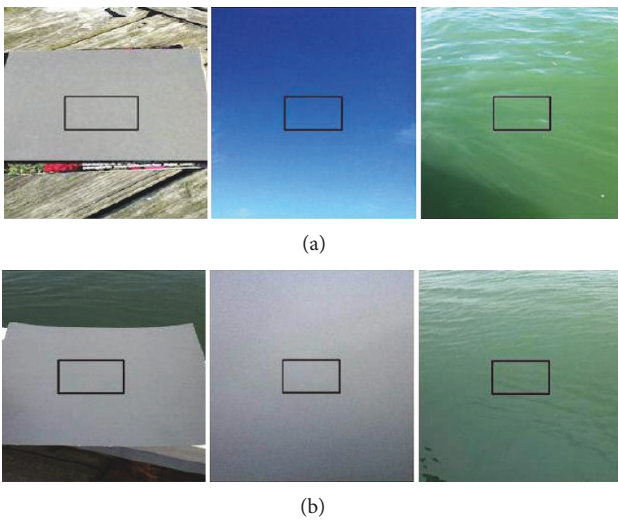


FIGURE 7: Sample gray card, sky, and water surface images taken on clear (a) and cloudy days (b) [40]. The rectangular area shows the selected representative true water colour.

the iPhone GPS and internal compass to predict the location of the sun in the sky. The compass is used to direct users to the correct azimuth angle, and the internal gyroscope directs users to the correct zenith angle [41]. The processing stages of the HydroColor App in summary comprises of the following steps:

- Colour image acquisition in terms of sRGB comprising of gray card, sky, and water surface colours
- Derivation of the relative radiances  $L_{rel} = RGB/\alpha_t$  of the acquired imagery, where  $\alpha_t$  is the camera's exposure time
- Conversion of  $L_{rel}$  to the top of atmosphere reflectance  $R_{rs}$ , where  $R_{rs} = (L_{water+surface} - \rho L_{sky}) / (\pi / R_{card} * L_{card})$  [41]. The radiances  $L$  are measured;  $R_{card}$  is the reflectance of the gray card (18%), and  $\rho$  is the fraction of skylight reflected by the surface ( $\sim 0.028$  at the azimuth and zenith angles used for the images).

- Conversion of  $R_{rs}$  to estimate the water quality parameters using the [40] algorithms as described below.

In deriving the water quality variables using the HydroColor app, the turbidity is first calculated and ranges between 0 and 80 NTU. The simplified model used by HydroColor to estimate turbidity from the red band reflectance  $R_{rs}(R)$  as proposed by [40] is expressed as in (14).

$$\text{Turbidity} = \frac{22.57 * R_{rs}(R)}{0.044 - R_{rs}(R)}. \quad (14)$$

From the turbidity estimates, the SPM is then obtained by deriving the relationship between turbidity in Formazin Turbidity Unit (FNU) and SPM, according to [40, 69], as expressed in (15).

$$\log_{10} \text{SPM} = 1.02 \log_{10}(\text{turbidity}) - 0.04. \quad (15)$$

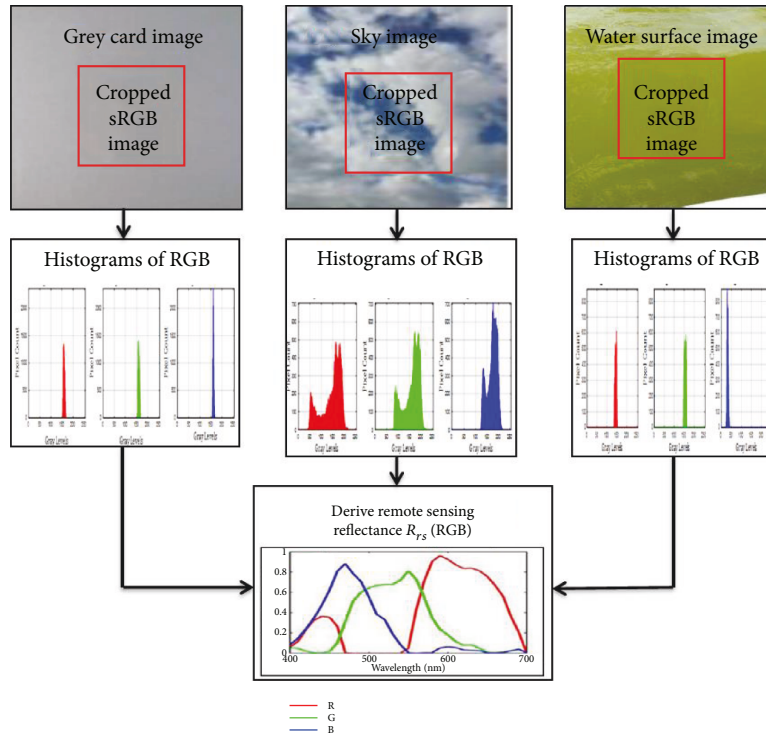
In determining the chlorophyll concentration using the HydroColor app, an adjusted ratio technique is first used, where the reflectance in the red is subtracted to calculate the Cchl-ratio as in (16) [40]. From the Cchl value, Chl-*a* is computed according to the exponential empirical function in (17).

$$\text{Cchl} = \frac{R_{rs}(B) - R_{rs}(R)}{R_{rs}(G) - R_{rs}(R)}, \quad (16)$$

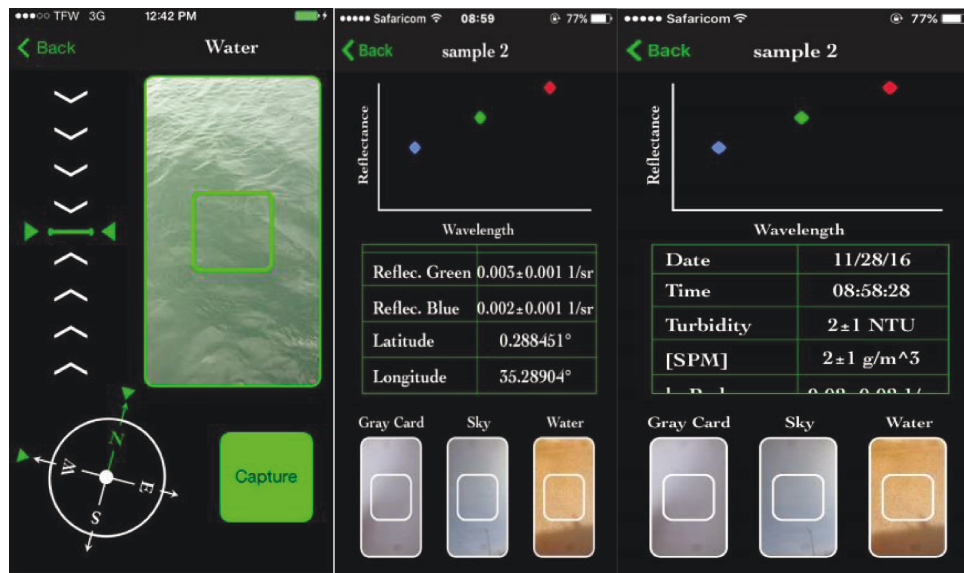
$$\text{Chl-}a = 3.09e^{-0.60\text{Cchl}}. \quad (17)$$

**3.3. Spatial Mapping of the Distribution of the Water Quality Parameters.** Within the reservoir surface water, detailed knowledge on the actual distribution of the water quality parameters is essential in interpreting and inferring accurate predictions of water quality in the entire water body. However, it is impossible to measure these phenomena at every point within a geographic area of the water body. By using an appropriate interpolation method on properly sampled data, the distribution and variability of water quality parameters can be accurately determined.

Although a variety of deterministic and geostatistical interpolation methods can be used to estimate variables at unsampled locations, accuracies vary widely among methods



(a)



(b)

FIGURE 8: Processing of water colour data using the HydroColor app to derive the  $R_{rs}$ (RGB) [40, 41] (a), and a screenshot of sample display results from PhytoBlog (b).

[70]. In order to estimate the distribution of WQP within a lake from discrete laboratory measurements, [71] compared inverse distance weighting (IDW), universal Kriging, and ordinary Kriging for interpolating the water quality parameters. Their results showed that the Kriging-based methods outperformed the IDW method by more than 10% in accuracy of interpolation. Obarrio [72] also obtained similar results in the investigation of lake water quality and its variability. Within the same case study area of

Kesses Dam, [73] compared the interpolation methods for elevation mapping and found that Kriging gave the best results. While there are several types of Kriging used in geostatistical data interpolation such as ordinary Kriging [74], universal Kriging [75], and median polish [76], ordinary Kriging is the basis of geostatistics and gives the optimal data predictions [71, 73], under the assumption that the process is second-order stationary with normal distribution [77].

To determine the interpolated value at some point in the parameter space, Kriging weights data samples that are nearby rather than giving all data samples of equal weight. The interpolation is achieved by setting the mean residual error to zero and also by minimizing the variance of the errors. Based on the concept of random functions, the surface or volume is assumed to be one realization of a random function with a certain spatial covariance [78]. The fundamental concept in Kriging interpolation therefore is to use the variogram to compute weights  $\lambda_i$ , which minimizes the variance in the estimated value. From a given data sample  $Z(x_i)$ , the semivariogram  $\gamma(h)$  can be estimated according to (18).

$$\gamma(h) = \frac{1}{2N(h)} \sum_{i=1}^{N(h)} \{Z(x_i) - Z(x_i + h)\}^2, \quad (18)$$

where  $\gamma(h)$  is the estimated semivariance at a separation distance or lag  $h$ ;  $Z(x_i)$  and  $Z(x_i + h)$  are the observed values at  $x_i$  and  $x_i + h$  separated by a distance  $h$ , of which there are  $N(h)$  pairs.

The semivariance tends to increase as the distance separating pairs of points (lag) increases, implying that points closer together tend to have more similar values than those far apart. Theoretical semivariogram fits can be based on spherical, exponential, Gaussian, and Bessel [73, 76]. In this study, the spherical model was chosen following from previous studies in which it yielded the best results [71, 73]. The general formula for the spatial interpolation is as given in (19), where  $Z^*(x_i)$  is the interpolated value at  $x_i$ .

$$Z^*(x_i) = \sum_{i=1}^{N(h)} \lambda_i Z(x_i). \quad (19)$$

Once the model variogram is fitted to the empirical data, it is used to compute the weights  $\lambda_i$ , such that the estimation variance is less than the variance for any other linear combination of the observed values [79]. With simple Kriging, one assumes that the mean value is known, while with ordinary Kriging the mean value is determined during the interpolation [80]. For nonstationary variation, where there is drift (or trend) in the data, universal Kriging or Kriging with intrinsic random functions should be used [81].

**3.4. Error Quantification for Water Quality Parameter Estimation.** In order to estimate the error between the WQP as determined from the laboratory measurements and estimated using the sensor-based empirical models, the following error estimators were adopted in this study, mean absolute error (MAE), root mean square error (RMSE), normalized root mean square error (NMSE), the coefficient of determination  $R^2$ , and the Pearson correlation coefficient  $r$ , and are summarized in Table 4. In Table 4,  $x_i$  and  $y_i$  are, respectively, the laboratory-measured (observed) and the predicted water quality parameters for each sample point  $i$ , and for the  $n$  samples. Regression scatterplots between the estimated and measured water quality parameters were also generated in order to visualize the correspondences between the models in terms of the water quality predictions.

TABLE 4: Summary of the WQP estimation error statistic.

Error estimator	Error equation
Mean absolute error or bias	$MAE = \frac{1}{n} \sum_{i=1}^n  x_i - y_i $
Root mean square error	$RMSE = \sqrt{\frac{1}{n} \sum_{i=1}^n (x_i - y_i)^2}$
Normalized root mean square error	$NRMSE\% = \frac{RMSE}{x_{i,max} - x_{i,min}} * 100$
Pearson correlation coefficient	$r = \frac{\sum_{i=1}^n (y_i - \bar{y}) \cdot (x_i - \bar{x})}{\sqrt{\sum_{i=1}^n (y_i - \bar{y})^2 \cdot \sum_{i=1}^n (x_i - \bar{x})^2}}$

TABLE 5: Laboratory spectrophotometric measurement results for Chl-*a* concentration.

Sample	(W-X) 664 <sub>b</sub> (nm)	(Y-Z) 665 <sub>a</sub> (nm)	(664 <sub>b</sub> - 665 <sub>a</sub> ) (nm)	Chlorophyll ( $\mu\text{g}\cdot\text{L}^{-1}$ )
1	0.7800	0.7443	0.0357	9.54
2	0.7170	0.6827	0.0343	9.15
3	0.6920	0.6600	0.0320	8.55
4	0.6081	0.5805	0.0276	7.37
5	0.4562	0.4343	0.0219	5.84
6	0.5871	0.5644	0.0227	6.05
7	0.7050	0.6711	0.0339	9.04
8	0.6088	0.5813	0.0275	7.35
9	0.8910	0.8525	0.0385	10.27
10	0.6532	0.6244	0.0288	7.69
11	0.8830	0.8449	0.0381	10.16
12	0.7950	0.7581	0.0369	9.84

## 4. Results and Analysis

### 4.1. Water Quality Parameter Measurements and Predictions

**4.1.1. Retrieval of Chlorophyll-*a* Concentration.** Using the spectrophotometric method [82], the results for the laboratory measurement and determination of the concentration of Chl-*a* in the twelve sampling stations are as presented in Table 5. The in situ measurement results show that the chlorophyll concentration in Kesses Dam ranged between 7 and 10  $\mu\text{g}\cdot\text{L}^{-1}$ , at the peak of the dry season.

From the Landsat data, the predefined algorithms in the second subsection of Section 3.2.1 were first used to determine the Chl-*a* concentration within the reservoir, by using the remote sensing reflectance  $R_{rs}$  as derived from band 2 (green) and band 4 (NIR). In carrying out the regression analysis between the Landsat-predicted and in situ laboratory measurements, the results in Figure 9 show an existence of a high correlation between the estimated and measured values for Chl-*a* of  $R^2 = 0.8111$ . This implies that the green band and the NIR band are instrumental in the detection of Chl-*a*, as also supported by results from studies by [8].

As already stated above, for HydroColor, an adjusted ratio technique is first used where the reflectance in the red

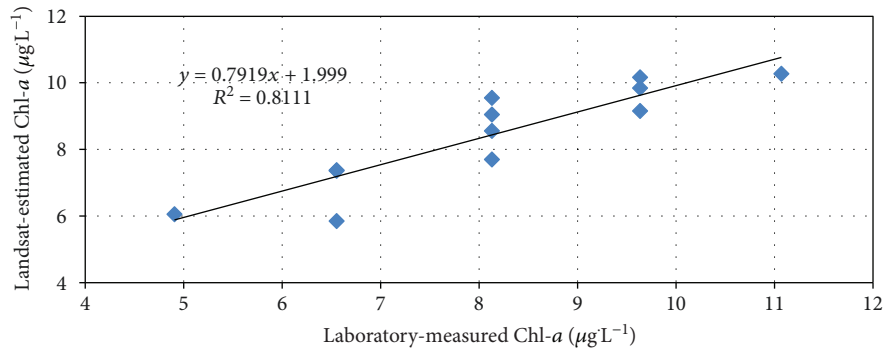


FIGURE 9: Correlation between Landsat-estimated and laboratory-measured Chl-*a*.

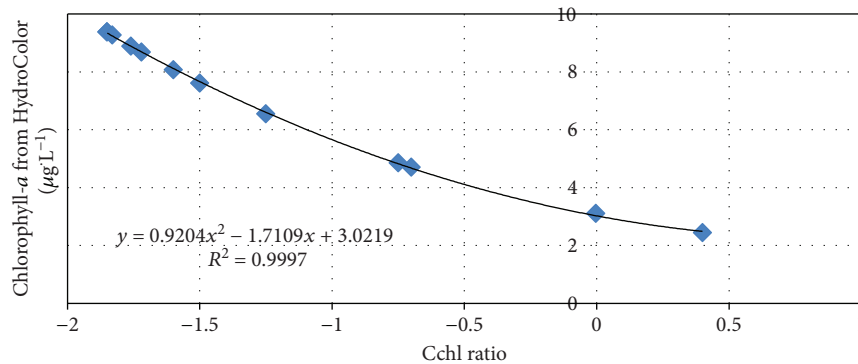


FIGURE 10: Relationship between the Cchl ratio and the estimated Chl-*a* concentration using the HydroColor app.

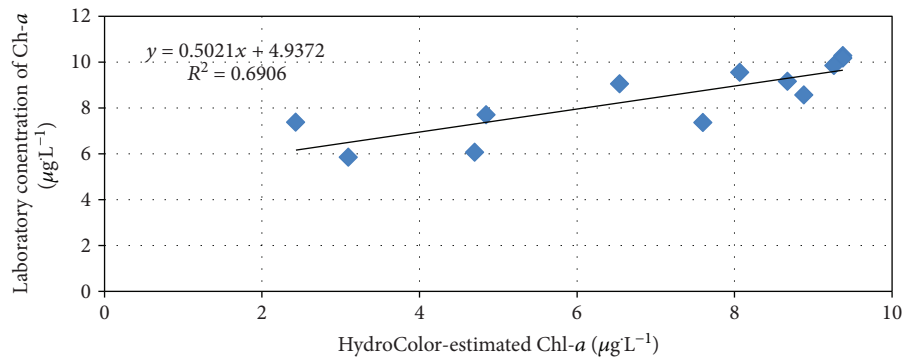


FIGURE 11: Comparison between laboratory-measured and HydroColor model estimation of Chl-*a*.

is subtracted before the Cchl parameter is used in the derivation of Chl-*a*. The surface values for extracted chlorophyll show a perfect relationship with the Cchl ratio as presented in Figure 10. The near 1 : 1 match validates the applicability of HydroColor for further data collection and analysis. The results of the regression between the laboratory measurements and the HydroColor estimates of Chl-*a* concentration are presented in Figure 11, and the results explain a coefficient of determination of nearly 0.7. A good correspondence between the in situ data and HydroColor in retrieving the concentration of chlorophyll in the reservoir is observed as depicted in Figures 10 and 11.

For the estimation of chlorophyll from EyeOnWater, the observed chlorophyll values were found to be quite negligible (in the order of  $\times 10^{-5}$ ) and could not be correlated with the

results from the laboratory measurements and other two models. These magnitudes of Chl-*a* as determined from EyeOnWater are attributed to the low values that are used in the calibration of the EyeOnWater model, as compared to the establishment laboratory observations. A regression between the chlorophyll concentration estimation results from Landsat and HydroColor showed a correlation of above 50% (Figure 12). In all the regression analyses, except for the validation of Cchl and Chl-*a*, the linear empirical model yielded the best regression fits.

A summary of the statistical analyses for the error quantifications between the laboratory measurements and the results from Landsat and HydroColor is presented in Table 6. From the summary results in Table 6, it is observed that for chlorophyll-*a* determination, there is an above



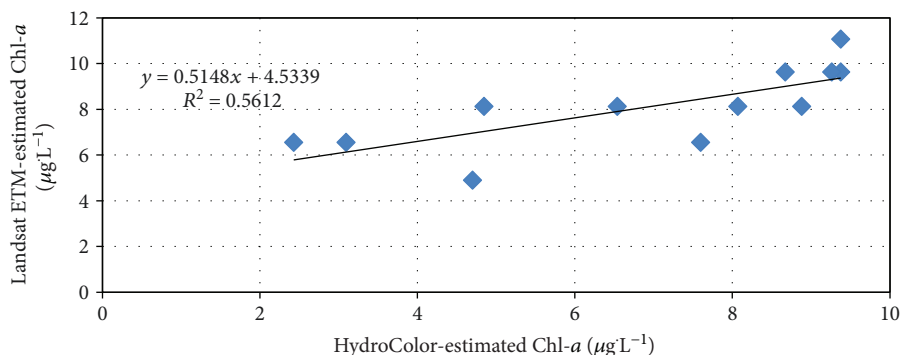


FIGURE 12: Correlation for Chl-*a* prediction using HydroColor and Landsat ETM+.

TABLE 6: Statistical summary of Chl-*a* estimations using Landsat and HydroColor models in relation to the in situ laboratory measurements.

Sensor	MAE (%)	RMSE ( $\mu\text{g}\cdot\text{L}^{-1}$ )	NRMSE1	NRMSE2	$r$	$R^2$
Landsat ETM+	0.7218	0.7900	0.1280	0.0980	0.9006	0.8111
HydroColor	20.925	2.0890	0.3010	0.3030	0.8310	0.6906

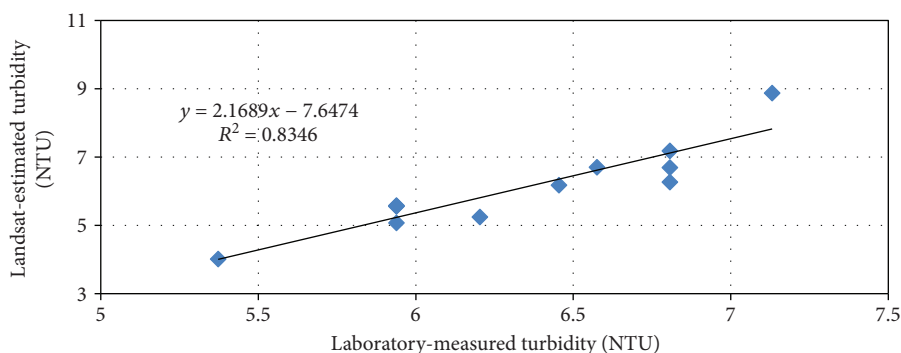


FIGURE 13: Estimated turbidity from Landsat as compared with the lab-measured turbidity.

average relationship between the Landsat-based model, the HydroColor app, and the measured data from laboratory testing. These results demonstrate that the Landsat- and HydroColor sensor-based models are significantly accurate and comparable in the estimation of the concentration of Chl-*a* in water reservoirs, with at least 70% degree of accuracy. In estimating Chl-*a* within the reservoir, it is observed that the Landsat-based model marginally performed better than HydroColor in terms of the RMSE and the coefficients of correlation and determination.

**4.1.2. Estimation of Turbidity.** The results from the laboratory measurements from the twelve sampling points showed that the degree of turbidity within the reservoir ranged between 5 and 8 NTU. For the regression analysis between the measured and predicted turbidity, the results are presented in Figures 13–15. Using linear and natural logarithmic empirical regression models, it is observed that all the three methods predicted the presence of turbidity by at least 70% accuracy as from the correlation coefficients. From the results of the estimation of turbidity from Landsat ETM+, the reflectance of the independent blue yielded the highest correlation coefficient. As in the case of Chl-*a* estimation, it can also be

concluded that the three models are suitable for predicting the presence of turbidity in inland waters.

To compare the results for the estimations of turbidity from the three models, an intermodel regression between the three WQP prediction results are presented in Figures 16 and 17. It is observed that for the single season analysis, Landsat and HydroColor are better in determining turbidity as compared to EyeOnWater. A statistical summary presented in Table 7 shows that for the models, the correlation coefficients are all higher than 0.8 in determining the turbidity. The MAE are observed to be at less than 5% on average, and the other error statistics are also much lower, all indicating good correlation between the apps and the reference laboratory measurements.

**4.1.3. Prediction of SPM.** From the laboratory test results, the reservoir was found to contain SPM concentrations ranging between 3 and 9  $\text{mg}\cdot\text{m}^{-3}$ . By using polynomial, natural logarithm, and linear regression models, the laboratory-measured SPM concentrations were empirically regressed with the Landsat, EyeOnWater, and HydroColor results for SPM prediction. The respective results presented in Figures 18–20 indicate that the coefficients of determination

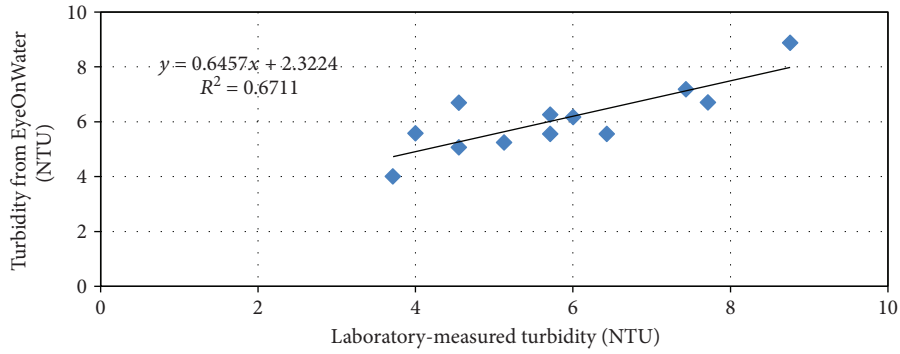


FIGURE 14: Regression model for turbidity from EyeOnWater and laboratory measurements.

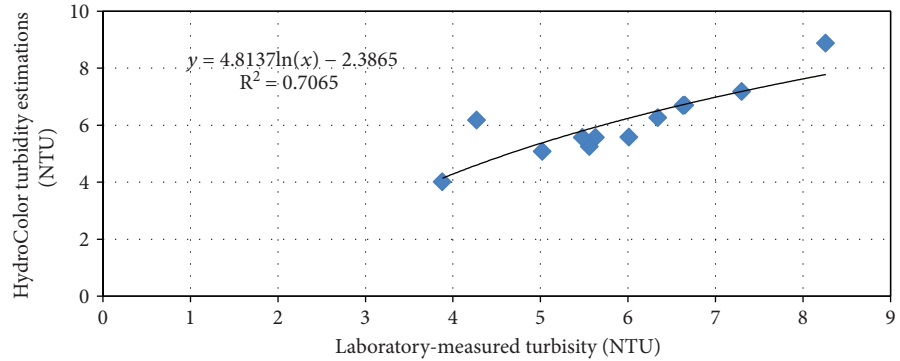


FIGURE 15: Relationship between HydroColor and laboratory testing for turbidity measurement.

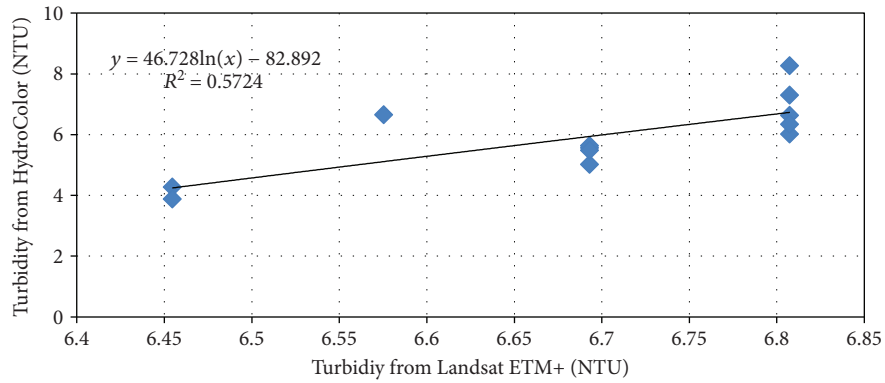


FIGURE 16: Performance evaluation for turbidity estimations from HydroColor and Landsat ETM+.

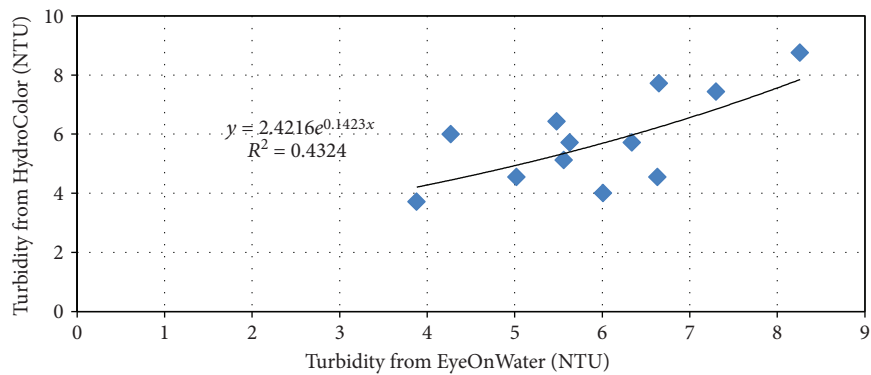


FIGURE 17: Performance correlation for turbidity estimations from HydroColor and EyeOnWater apps.

TABLE 7: Statistical analysis of the prediction of turbidity using Landsat ETM+, EyeOnWater, and HydroColor app models.

Sensor	MAE (%)	RMSE (NTU)	NRMSE1	NRMSE2	<i>r</i>	<i>R</i> <sup>2</sup>
Landsat ETM+	0.624933	0.7920	0.4510	0.1250	0.9136	0.8346
EyeOnWater app	4.623951	0.8970	0.1780	0.1543	0.8190	0.6711
HydroColor app	5.250214	0.6010	0.1240	0.1014	0.8405	0.7065

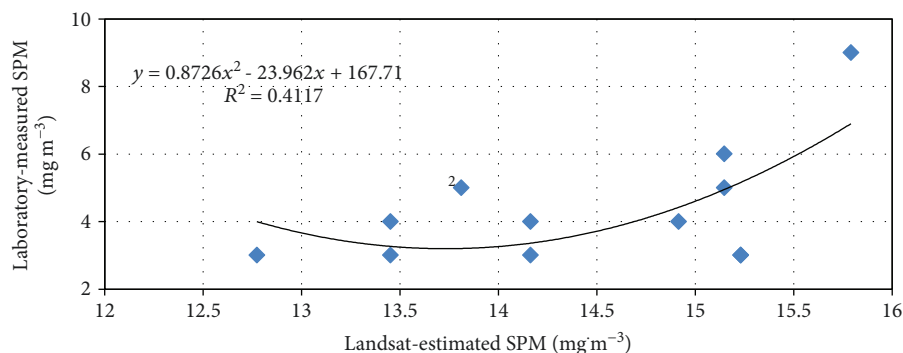


FIGURE 18: Laboratory-measured SPM versus the Landsat-estimated SPM.

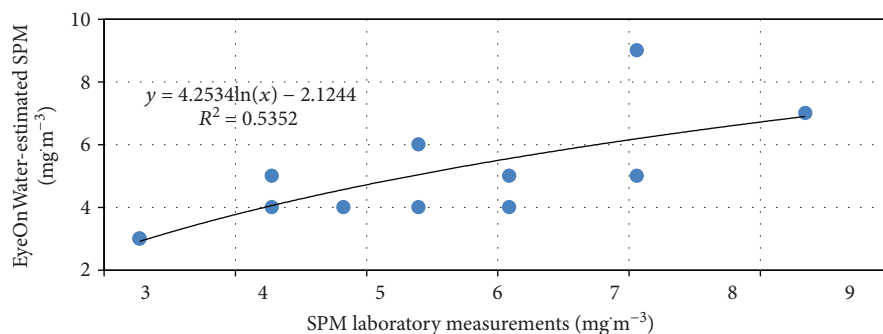


FIGURE 19: Comparison of predicted SPM from EyeOnWater app and laboratory measurements.

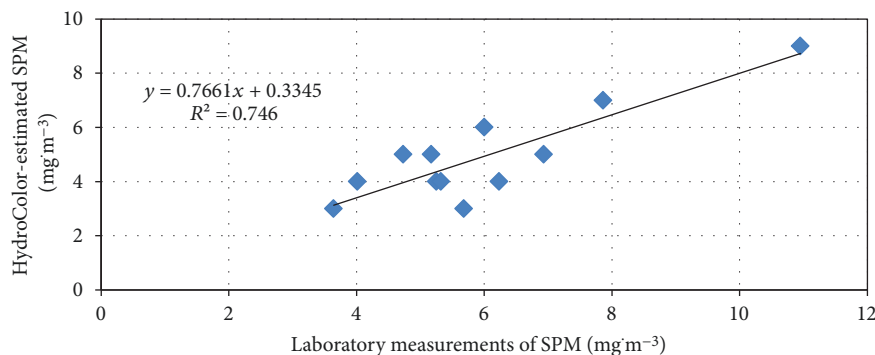


FIGURE 20: Correlation of results of SPM from HydroColor and laboratory testing.

were determined 0.4117, 0.5352, and 0.7460. The results from Landsat indicate that the ETM+-band 2 (green) and band 4 (NIR) may not be the best in estimating the SPM concentration as the coefficient of determination was at below 50%. The results show that both the EyeOnWater and HydroColor apps are suitable for determining the concentration of SPM, with the best SPM determinant being from the HydroColor app.

The results of intercorrelational analysis for the determination of SPM from Landsat and the two apps, as shown in Figures 21 and 22, illustrate the fact that for SPM determination, the models present differing results. However, a summary in Table 8 of the statistical analysis shows that all the models except for Landsat are capable of detecting the presence of SPM with more than 50% of accuracy as determined using the coefficient of determination. Despite the fact that

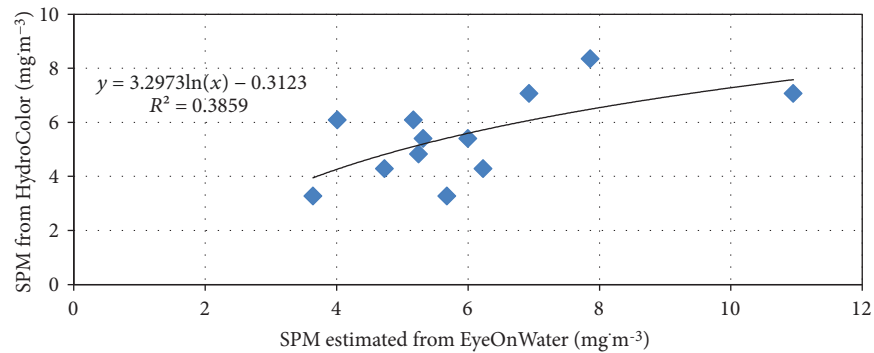


FIGURE 21: Intercorrelational analysis of SPM estimation from HydroColor and EyeOnWater apps.

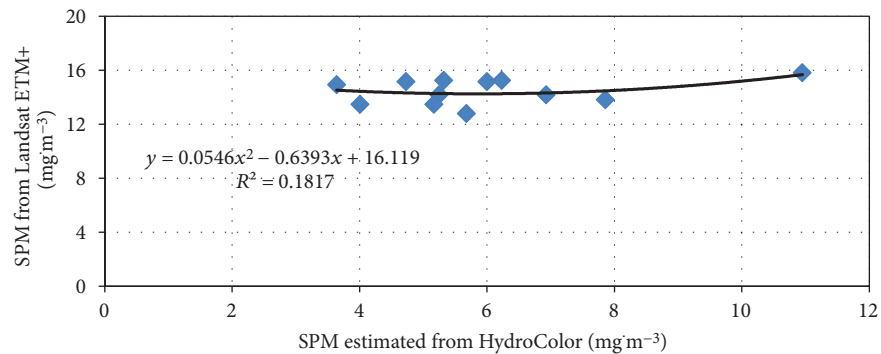


FIGURE 22: Correlation of results of SPM from HydroColor and laboratory testing.

TABLE 8: Statistical evaluation of SPM estimation using Landsat, EyeOnWater, and HydroColor App models.

Sensor	MAE (%)	RMSE ( $\text{mg}\cdot\text{m}^{-3}$ )	NRMSE1	NRMSE2	$r$	$R^2$
Landsat ETM+	10.11	10.478	4.4820	0.7260	0.6416	0.4117
EyeOnWater app	4.06	1.2612	0.3140	0.2360	0.7315	0.5352
HydroColor app	26.02	1.4212	0.1940	0.2380	0.8637	0.7460

HydroColor had the highest MAE of 26%, the regression coefficients are much higher as compared to the Landsat and HydroColor estimates. Notably, the SPM estimates from the three models are observed to have high predictive differences, hence the low regression coefficients.

As already mentioned in the introduction, the discrimination of SPM from water reflectance is based on the relationship between the scattering and absorption properties of water and its constituents. Most of the scattering is caused by suspended sediments, and the absorption is controlled by chlorophyll-*a* and coloured dissolved organic matter. These absorptives in water components have been shown to lower the reflectance in a substantial way, and their effects are generally found at wavelengths less than 500 nm [10].

**4.1.4. Prediction of Water Colour.** The colour of water is a classic relative indicator that has been instrumental in detecting harmful algal blooms, release of contaminants, and track plumes [5, 83]. Observations of water colour can be carried out using near-water surface, airborne, and satellite platforms. The colour saturation of a water system determines

how much optically active components are present to apparently affect the measure of the depth of light penetration into the water. Colour saturation as a quantitative measure of the saturation of a particular colour does not depend on the type of water constituent but on the constituents' capability to attenuate light. In this case study, the colour saturation and the dominant water colour wavelength for each sampling point measurement were obtained with the results summarized in Table 9 for the inferred laboratory measurements, and from EyeOnWater and HydroColor inferences.

Because it is not possible to retrieve the water colour from Landsat ETM+ bands in terms of wavelengths, and for comparison with the laboratory-based colour wavelengths, only results from the laboratory measurements, EyeOnWater, and HydroColor are presented. The results in Table 9 indicate that the water wavelength colour in the reservoir varied between 500 and 590 nm. Using the laboratory colour chart as the reference, it is inferred from Table 9 that the EyeOnWater colour FU results were comparable to the standard laboratory wavelengths. For the HydroColor, the app's colour reference scheme is different from the standard laboratory scheme; thus, as seen in Table 9, the wavelengths are

TABLE 9: Summary of colour measurements using laboratory spectrophotometry, EyeOnWater, and HydroColor apps.

Sampling station	1	2	3	4	5	6	7	8	9	10	11	12
Laboratory wavelength (nm)	550	570	550	500	570	500	500	570	500	530	580	550
Laboratory colour hue	Greenish-yellow	Greenish-yellow	Greenish-yellow	Green	Greenish-yellow	Green	Green	Greenish-yellow	Green	Green	Yellow	Greenish-yellow
EyeOnWater FU values	12	13	10	8	11	15	8	13	14	9	11	9
EyeOnWater wavelength (nm)	550	570	550	500	570	500	500	570	500	530	590	550
EyeOnWater colour hue	Greenish	Greenish	Greenish	Greenish-blue	Greenish	Greenish-brown	Greenish-blue	Greenish	Brownish-green	Bluish-green	Greenish	Greenish-blue
HydroColor wavelength (nm)	553	513	553	553	553	490	609	553	553	553	513	513
HydroColor colour hue	Greenish-brown	Greenish	Greenish-brown	Greenish-brown	Greenish-brown	Greenish-blue	Orange-green	Greenish-brown	Greenish-brown	Greenish-brown	Greenish	Greenish

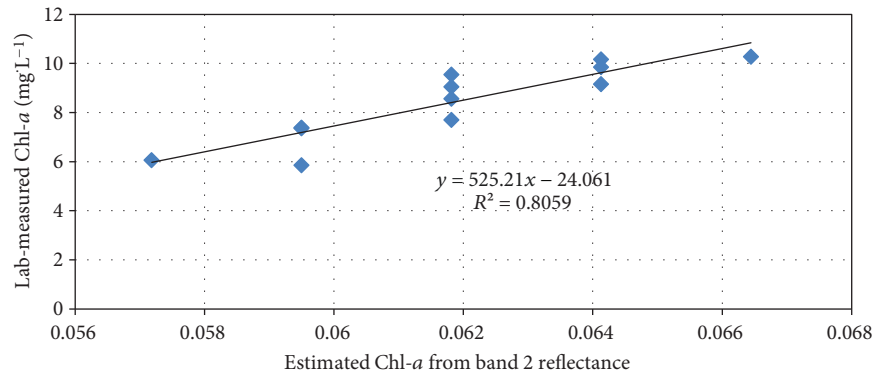


FIGURE 23: Comparison and regression of Chl-*a* estimates from  $R_{rs}(G)$  and measured from lab testing.

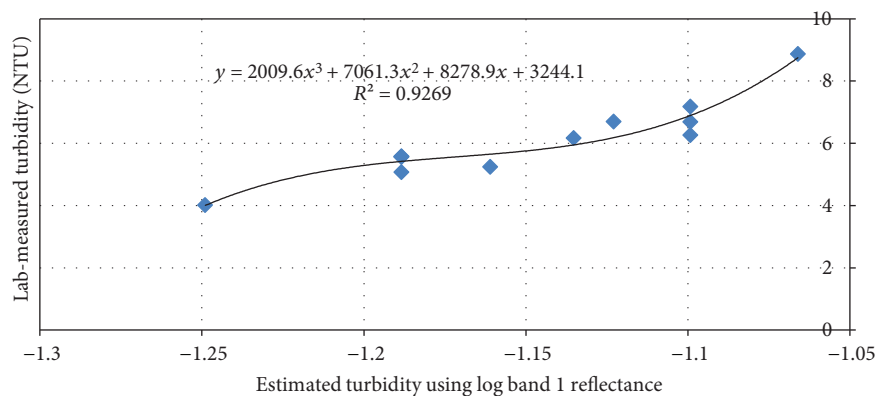


FIGURE 24: Regression of predicted from  $R_{rs}(B)$  and measured turbidity.

in the range of 513–609 nm. Similar findings were also made by [44].

The results in Table 9 show that the dominant water colour in the reservoir is the greenish colour. By inference, predominantly greenish water colour indicates increased nutrient and phytoplankton levels, as well as a high content of minerals and dissolved organic materials. Greenish-blue is also an indication of algae dominance, and increased dissolved matter and sediments may be present. The greenish-brown colour characterizes high nutrient and phytoplankton concentration and increased sediment and dissolved organic matter. It implies that if the water looks especially green, then there are a lot of microscopic algae (phytoplankton) growing near the surface. Phytoplankton blooms often turn the water green, but a dense bloom of certain species can be orange, brown, or red. When the water looks murky and brown, it means there are sediments or mud suspended in the water.

**4.2. Development of Predictive Model WQP Retrieval from Landsat ETM+-VNIR.** While several studies have developed algorithms for water quality retrieval, the main challenge in using already existing algorithms, as already stated, is that the conditions of sample collection and the specific dynamics and characteristics of water bodies vary significantly. Also, in developing the algorithms, the spectral characteristics, reflectance, radiance, and pixel resolution values are often regressed against the laboratory-acquired results. The results

of the empirical regression analysis and generation of the WQP predictive models are represented in Figures 23–25, and a summary of the correlational analyses of the Landsat ETM+-VNIR bands in generating the case study algorithms is presented in Table 10.

From the results, it is observed that the independent variables comprising of ETM+-band 2 (green) and band 3 (red) had the highest significant relationships in estimating the presence of chlorophyll-*a*, as they, respectively, explained 90% and 66% of the correlation accuracy (Table 9). From the results in Figures 9 and 23, it is deduced that Chl-*a* in the Kesses Dam case study can effectively be predicted using the new regression model that is based on the remote sensing reflectance of ETM+-band 2, with  $R^2$  of 0.8059. The results are comparable to that of the tested [23] algorithm and are represented by a simple linear regression equation of the Landsat ETM+ green band.

For the derivation of Chl-*a* from Landsat, the broad ETM+/TM bands may not spectrally resolve the sharp spectral features arising from the absorption by Chl-*a*. This is because chlorophyll comprises of the combined biological, physical, and chemical factors, making the spectral patterns complex. The Chl-*a* absorption peak is in the red region of the spectrum at 670 nm which is only half contained in the red band of ETM+ data; the peak near 700 nm is out of the ETM+ red band. Therefore, different methods of band combinations from band 2 and band 4 may be applied to the

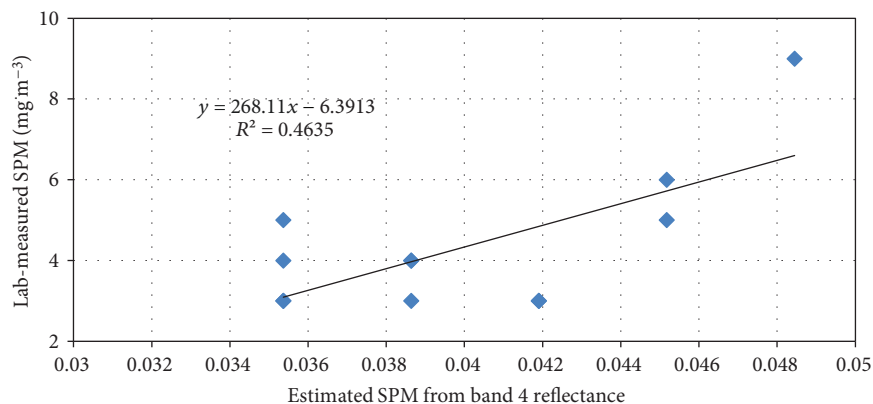


FIGURE 25: Regression of predicted SPM concentration from Landsat ETM+-band 4 reflectance and sampling measurements.

TABLE 10: Bivariate regression equations and the corresponding correlation coefficients for WQP estimations from Landsat ETM+ bands.

Water quality parameter	Remote sensing reflectance $R_{rs}(\lambda)$	Bivariate regression models ( $x = R_{rs}(\lambda_i)$ )	$r$	$R^2$
Chl- <i>a</i>	$R_{rs}(R)$	$y = 385.93x - 7.4615$	0.6596	0.4351
	$R_{rs}(G)$	$y = 525.21x - 24.061$	0.8977	0.8059
Turbidity	$R_{rs}(\log_{10}B)$	$y = 2009.6x^3 + 7061.3x^2 + 8278.9x + 3244.1$	0.9628	0.9269
	$R_{rs}(B)$	$y = 3092.4x^3 - 14585x^2 + 22940x - 12027$	0.9629	0.9272
	$R_{rs}(G)$	$y = -64775x^2 + 8009.5x - 241.12$	0.3971	0.1577
	$R_{rs}(R/NIR)$	$y = -28.676x^2 + 62.138x - 27.139$	0.3173	0.1007
SPM	$R_{rs}(B/G)$	$y = 5.6364x^2 - 22.611x + 26.351$	0.3790	0.1440
	$R_{rs}(NIR)$	$y = 0.7278x^2 - 16.75x + 99.462$	0.6808	0.4646
	$R_{rs}(R/NIR)$	$y = 54.665x^2 - 120.24x + 69.507$	0.5234	0.2739
	$R_{rs}(R)$	$y = 0.376x^2 - 18.492x + 230.42$	0.4511	0.2035

ETM+ data to determine the Chl-*a* level [84]. The findings in this study for the Chl-*a* regression is also supported by the study results from [85], where it was demonstrated that chlorophyll-*a* could be retrieved using models based on the red or green band, with the model with the green band giving the most optimal results. The results for Chl-*a* determination are also supported by the experimental analysis by [8], where by simulating the OLI bands in order to estimate Chl-*a*, high absorption at the green band and low absorption at the blue region were associated with the presence of chlorophyll-*a*.

Water turbidity is caused by the presence of suspended and dissolved matter such as clay, silt, finely divided organic matter, plankton, other microscopic organisms, organic acids, and dyes [53]. Because of these constituents, turbidity is an indicator and measure of the light-scattering properties of water. From the experimental results, it was observed that the independent variables comprising of the logarithm of ETM+-band 1 had the most significant relationship with turbidity, as it explained more than 92% of the variance in turbidity (Figure 24). Using a cubic polynomial regression model, the results in Figure 24 show that  $R_{rs}(B)$  is more suitable in estimating the turbidity in the reservoir as compared to the logarithmic band ratio results in Figure 13, from [26]. Notably from Table 10, the results from the remote sensing

reflectance are seen to be same as those from the natural log of ETM+-band 1. Again, it is deciphered here that the independent blue-band variable is the most suitable band for the prediction of turbidity.

From the literature review, most remote sensing studies have been devoted to retrieve SPM, which is the parameter of main interest in sediment transport studies; however, fewer studies have been dedicated to the retrieval of turbidity. Nonetheless, turbidity has been used as an effective indicator of water quality, and being an optical property of water, it is more strongly related to the backscattering coefficient and thus to reflectance than is SPM. In this study, the correlation analysis between the in situ measured SPM and the Landsat-derived  $R_{rs}(\lambda)$  for SPM estimation indicated that there was a significant positive correlation between the ETM+-derived reflectance in the near-infrared  $R_{rs}(NIR)$ , exhibiting a fair correlation of  $R^2 = 0.4635$  and  $r = 0.6808$  at  $p < 0.05$ , with the in situ SPM measurements using a linear regression model (Figure 25). This relatively low correlation between the in situ measurement of SPM and the ETM+-based derived  $R_{rs}(NIR)$  is also reported in related studies (e.g., [86–91]). It can be concluded that because SPM transports nutrients and contaminants, it reduces the transmission of light through a water column hence influencing the entire

aquatic ecosystems [92]. This means that it may be more complex to detect SPM in the VNIR as also reported in the empirical results by [23].

From the results in Figures 23–25, it is conclusive that the ETM+-VNIR bands can effectively be used for the estimation of the turbidity and Chl-*a*; however, further research needs to be carried out on the use of the Landsat bands in the more accurate detection of the SPM in reservoirs. A summary of the empirical regression correlation equations is presented in Table 10. Only the results that meet the set criteria of the significance  $p < 0.05$  are presented.

The determination of the trophic status of reservoir and lakes is one of the prime inland water management issues, and the trophic state is often characterized by the Chl-*a* and SPM. From the case study results presented above, it is evident that the reservoir WQP can be estimated using the EyeOnWater and HydroColor smartphone apps and the Landsat ETM+-VNIR bands. For monitoring the local water bodies, the results show that the smartphones are most suitable for estimating all the three WQP with an accuracy of above 75% in terms of the correlation coefficients, except in using EyeOnWater for predicting the presence and concentration of chlorophyll. Landsat on the other hand is most appropriate in measuring all the three water quality parameters with very high accuracy of up to 90% for Chl-*a* and turbidity, and 68% accuracy for SPM in terms of the determined correlation coefficients  $R$ . The results are all positively showing the applicability of smartphone apps and the Landsat ETM+-VNIR in obtaining the WQP in a reservoir.

Previous studies have also indicated that the use of single bands gave better results for the estimation of the analyzed water quality physical parameters. Hicks et al. [93] generated Pearson correlation coefficients between  $-0.46$  and  $0.96$  for turbidity for lakes in New Zealand using Landsat 7 and reported strongest relationships ( $>0.90$ ) for single bands blue, red, and NIR.

**4.3. Evaluation of the Spatial Distribution and Variability of the WQP in the Reservoir.** In order to further analyze the performance of the models and to estimate the spatial distribution and variability of the predicted and estimated reservoir water quality parameters, spatial interpolation was carried out using ordinary Kriging as explained above. By determining the spatial distributions of the water quality variables, it is possible to analyze, characterize, and visualize the water quality over the entire reservoir from the sample points.

**4.3.1. Distribution and Variability of Chl-*a*.** The results for the spatial interpolation of the measured concentrations of Chl-*a* are presented in Figure 26, with Figure 26(a) showing the benchmark Chl-*a* distribution results from the laboratory measurements. Apart from the results from EyeOnWater (Figure 26(d)), which as already mentioned above have different calibration values, the results from Landsat and HydroColor (Figures 26(b) and 26(c)) show matching results with those from the laboratory measurements in Figure 26(a). It is observable that the areas with the highest and lowest concentrations of Chl-*a* are in good coincidence

not only in relative location and distribution but also in terms of the magnitudes of the concentrations of chlorophyll within the reservoir. For example, in the case of laboratory measurements, the maximum ranges of Chl-*a* concentration are observed to be between  $7.37$  and  $10.3 \mu\text{g}\cdot\text{L}^{-1}$ , while the maximum Chl-*a* concentration results from Landsat estimates range between  $7.75$  and  $11.1 \mu\text{g}\cdot\text{L}^{-1}$ , and similarly for HydroColor the range was between  $7.72$  and  $9.38 \mu\text{g}\cdot\text{L}^{-1}$ . These results illustrate the fact that the presence and concentration of Chl-*a* can be estimated using both Landsat, by using the developed regression model equation, and the HydroColor App. A similar trend in the location and distribution patterns of areas with the least Chl-*a* concentrations is observed to coincide with the laboratory-measured results.

From the results in Figures 26(a)–26(c), the areas exhibiting the highest concentrations of Chl-*a* correspond to areas which receive water via the two streams, which pass through the agricultural lands and villages in adjoining areas of the dam and within the watershed. Also towards the weir, there is high activity which is mainly due to the agricultural activities in the nearby farms. The rest of the reservoir waters show fairly lower concentrations of Chl-*a*, as they are further away from the main point and nonpoint sources of pollutants.

**4.3.2. Turbidity Distribution.** The turbidity was measured from laboratory measurements and estimated from the Landsat, EyeOnWater, and HydroColor models. The results for the spatial mapping from the point turbidity estimates are presented in Figure 27. Similar to the distributions observed for chlorophyll, turbidity also exhibited similar variability patterns for the four spatial maps. It is observable in Figure 27 that the maximum and minimum ranges of turbidity are similar, with nearly the same locational distributions. Notable however is that the regions with high concentrations in chlorophyll are not the same as those with high turbidity levels. However, the reservoir areas with low chlorophyll concentrations are the same as for turbidity levels.

**4.3.3. Spatial Mapping of SPM.** The distribution patterns of SPM within the inland water body systems are important in understanding its ecosystem dynamics and for the development of effective and quantitative monitoring of aquatic environments [94, 95]. The results for the spatial interpolation and distribution mapping of SPM using Kriging are as presented in Figure 28. While the laboratory results exhibited only five major SPM concentration ranges from the twelve sampling points (Figure 28(a)), the three sensor-based models showed more variations in terms of the SPM concentrations within the dam. The pattern, magnitude, and trend of the distribution of SPM within the dam as determined using Landsat and EyeOnWater (Figures 28(b) and 28(c)) are observed to be similar to the generated patterns from the in situ observations in Figure 28(a). The same trend in the magnitude and spatial distribution is also observed from the HydroColor results in retrieving the concentration of SPM (Figure 28(d)), with slight variations especially in the areas of high SPM concentrations.



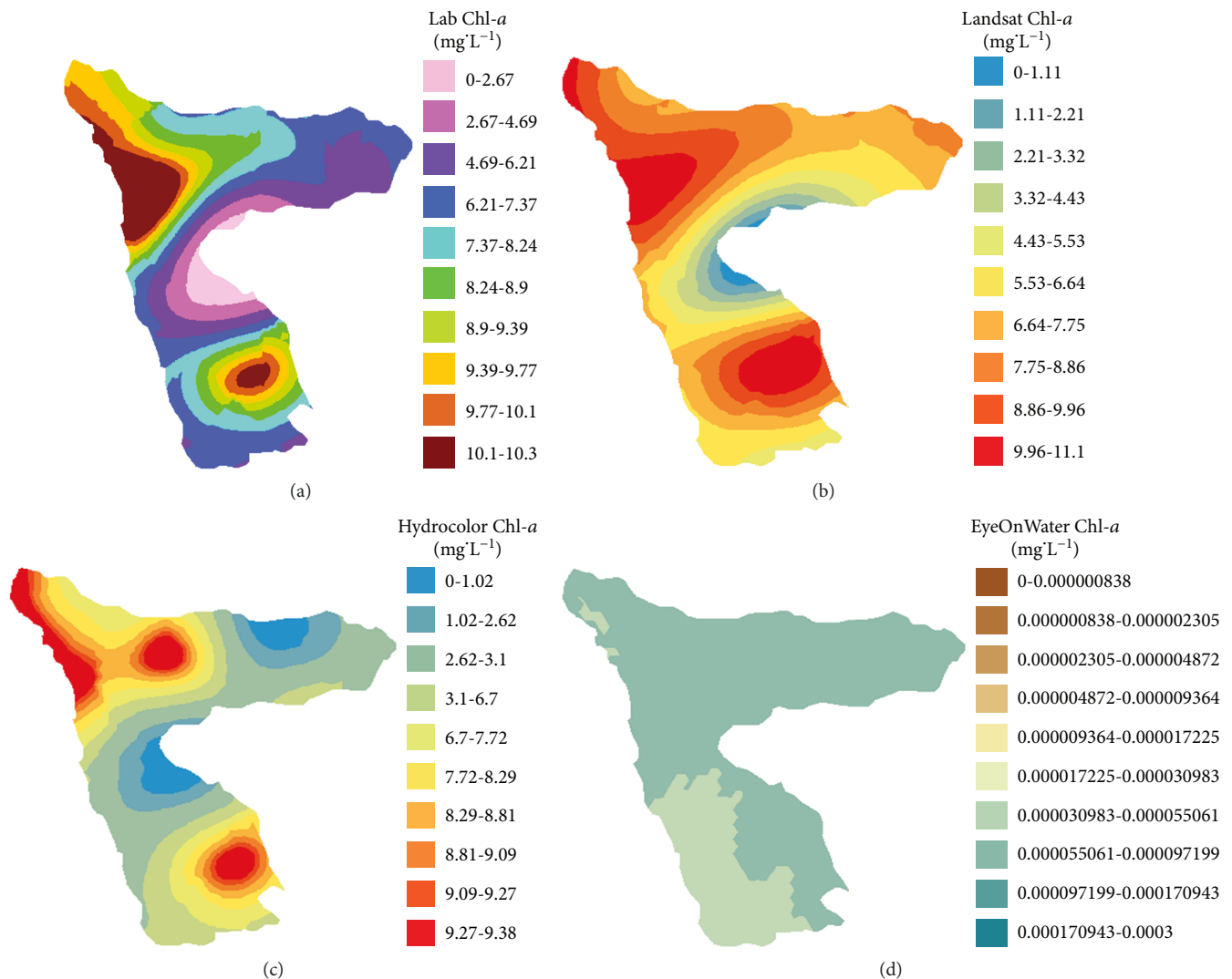


FIGURE 26: Spatial maps of chlorophyll-*a* distribution from (a) laboratory measurements, (b) Landsat data, (c) HydroColor, and (d) EyeOnWater.

**4.3.4. Water Colour Mapping.** For the spatial interpolation of the determined water colour wavelengths within the reservoir, it was possible to generate the distribution maps from the laboratory measurements and the smartphone apps, with the results shown in Figure 29. In comparing the results from the in situ measurements (Figure 29(a)) with the EyeOnWater results in Figure 29(b), it is noticeable that the maxima and minima wavelengths are in coincidence in magnitude and in spatial location; hence, EyeOnWater accurately detected the reservoir water colour.

For the HydroColor app, there was a generation of the colour hue and not the actual value for the water colour in terms of wavelength. Because HydroColor uses different colour charts from the conventional charts for laboratory testing, it was not possible to directly correlate the results for colour between HydroColor and laboratory results. Trial results correlating the HydroColor colour hues to the wavelength are given in Figure 29(c). Despite the differences in magnitude of wavelengths between the laboratory and the HydroColor results, there is an observed good correlation

of the water colour especially in the lower and dominant wavelengths. The spatial distribution patterns of the water colour from the two apps are also observed to be in agreement with that of the in situ reference. Of significant interest is the observed coincidence between the mapped Chl-*a* variability maxima and minima with those of the water colour. It is concluded that there is a strong evidence of correlation between the water colour and the presence of chlorophyll within the water reservoir system.

In general, the results from this study may not be as strong due to the unique reservoir morphology and water composition, which can be attributed to the reservoir system turnover effect, when the equalization of the thermal gradient in the reservoir induces mixing of surface and bottom waters, making remote monitoring difficult due to instability [60]. However, the main contribution of this research is that the automated processing methodology allowed for the processing and analysis of selected physical water quality parameters using the in situ laboratory assessments, and radiance analysis of Landsat ETM+ and smartphone camera

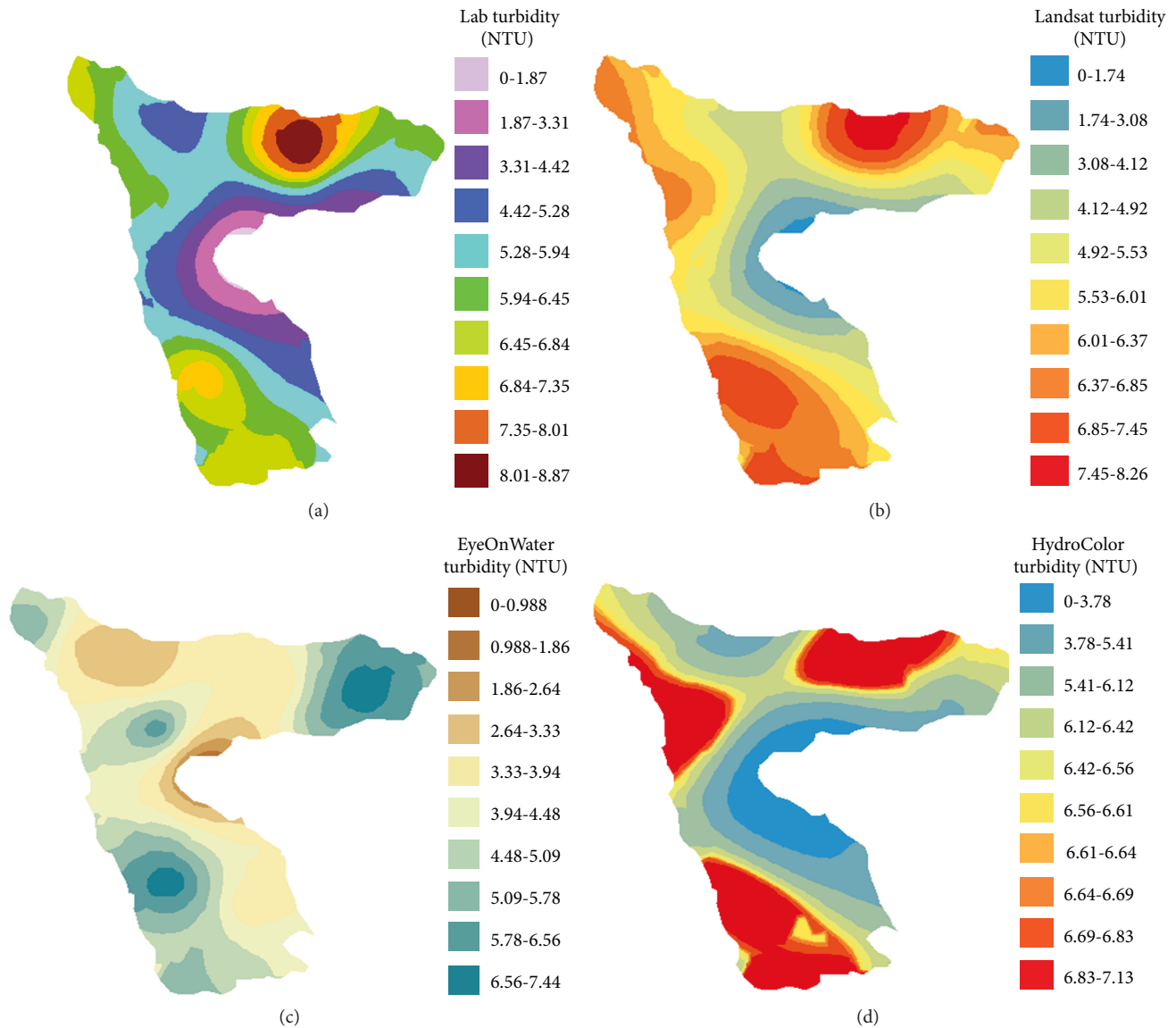


FIGURE 27: Turbidity distribution maps from (a) laboratory measurements, (b) Landsat, (c) EyeOnWater, and (d) HydroColor.

observations, with significant potential for rapid water quality analysis, and for the involvement and encouragement of citizens to participate in environmental resource monitoring, such as water quality assessments and reporting using state-of-the-art techniques including smartphone apps and satellite data [28, 32–34].

## 5. Conclusions

The conventional laboratory-based methods for monitoring water quality not only are cost-ineffective but also do not represent the synoptic and spatial-temporal view of the quality of surface water in time and space. Because of the rapidly growing societal awareness on the changes in the environment and climate, there is a parallel need to engage citizens in gathering relevant scientific information for monitoring environmental changes, such as water supply and quality, due in part to the recognition that citizens

are a potential source of such critical information [34]. The developments in optical and thermal sensors have made remote sensing to be an effective tool for extracting spatial-temporal information on water quality. This study presented the results of a comparative evaluation of three sensor-based models from Landsat ETM+-VNIR data and two smartphone apps—EyeOnWater and HydroColor—for rapid and cost-effective prediction of optically active water quality parameters as characterized by turbidity, chlorophyll-*a*, water colour, and SPM, with a case study of Kesses Dam in Kenya.

The results from the three models are compared with the in situ laboratory measurements by using empirical regression modelling and spatial interpolation using ordinary Kriging. For the estimations of SPM and Chl-*a* from ETM+, Laili et al.'s [23] algorithms were first used for comparative evaluation and analysis, and the results showed that the concentrations of the two WQP were estimated with a coefficient

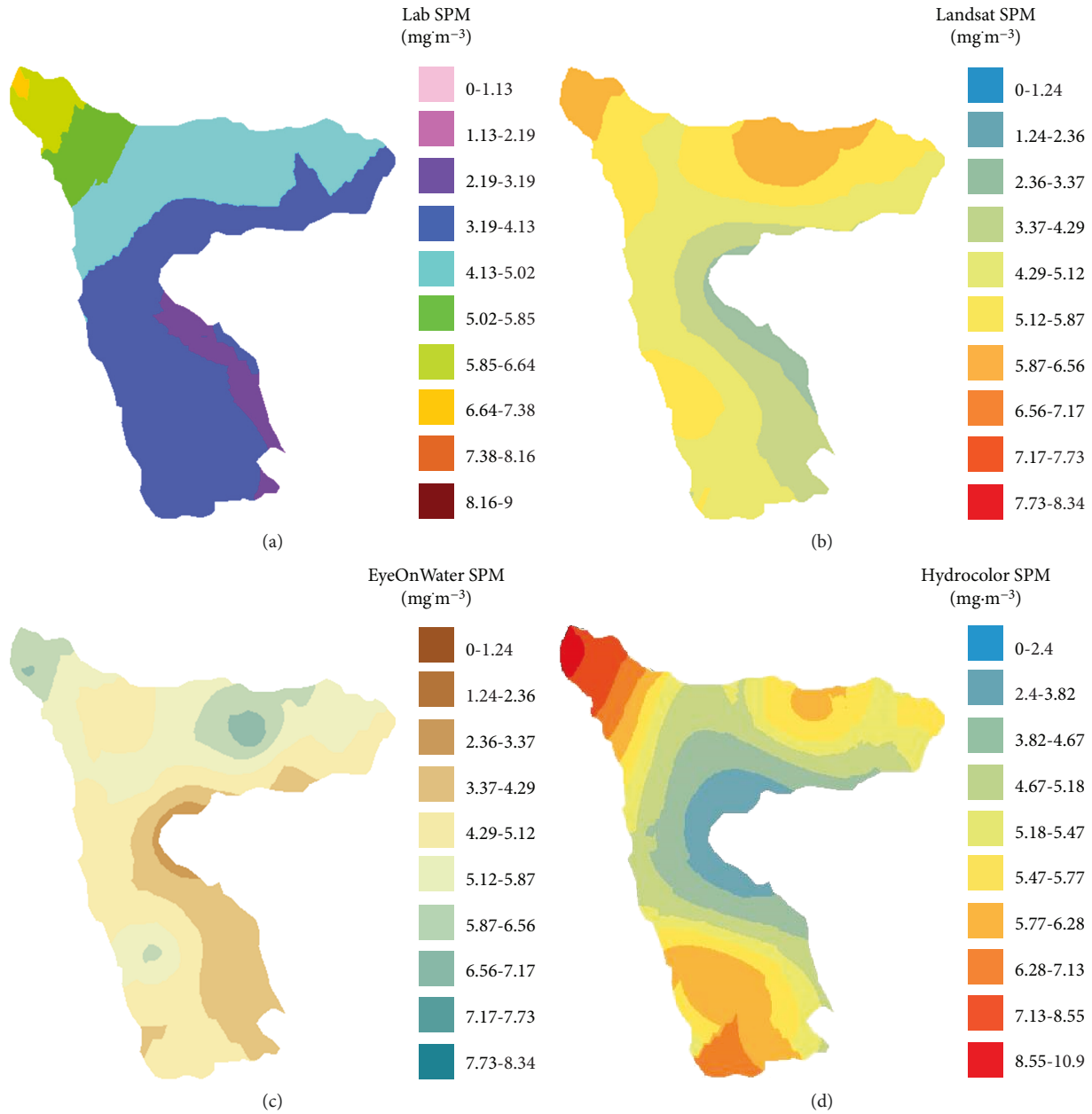


FIGURE 28: Concentration maps of SPM: (a) laboratory measurements, (b) Landsat, (c) EyeOnWater, and (d) HydroColor.

of determination of  $R^2 = 0.4117$  for SPM and  $R^2$  of 0.8111 for Chl-*a*. For the initial turbidity estimation within the dam, Waxter's [26] algorithm estimated the degree of turbidity with  $R^2 = 0.8346$ . In order to determine the suitable case study functions for detecting the water quality parameters from the Landsat ETM+ bands, regression modelling and analysis between the ETM+ bands and the laboratory-measured water quality variables were carried out. For the retrieval of Chl-*a*, a linear empirical model from the remote sensing reflectance with ETM+-band 2 gave the best results, with a Pearson correlation coefficient of 0.8977. Using a cubic polynomial linear regression model, the best measure for turbidity was obtained from the independent ETM+-band 1 reflectance with  $R > 0.9$ . For the estimation of SPM, a

second-order polynomial using the ETM+-NIR band gave the best results with Pearson correlation of  $r = 0.6808$ .

The EyeOnWater app, which observes the optical colour of water based on the Forel-Ule index, presents an easy and convenient approach of acquiring and displaying real-time information about water quality parameters. By using the initial regression models for the estimation of turbidity and SPM, the two WQP were, respectively, estimated with coefficients of correlation  $r = 0.819$  and  $r = 0.7315$ . For the HydroColor app, the two variables were determined with respective Pearson correlation coefficients of 0.8405 and 0.8637 for turbidity and SPM. Comparatively, the estimation of turbidity from the EyeOnWater app, which is based on the FUI-XYZ colour space, was marginally lower than

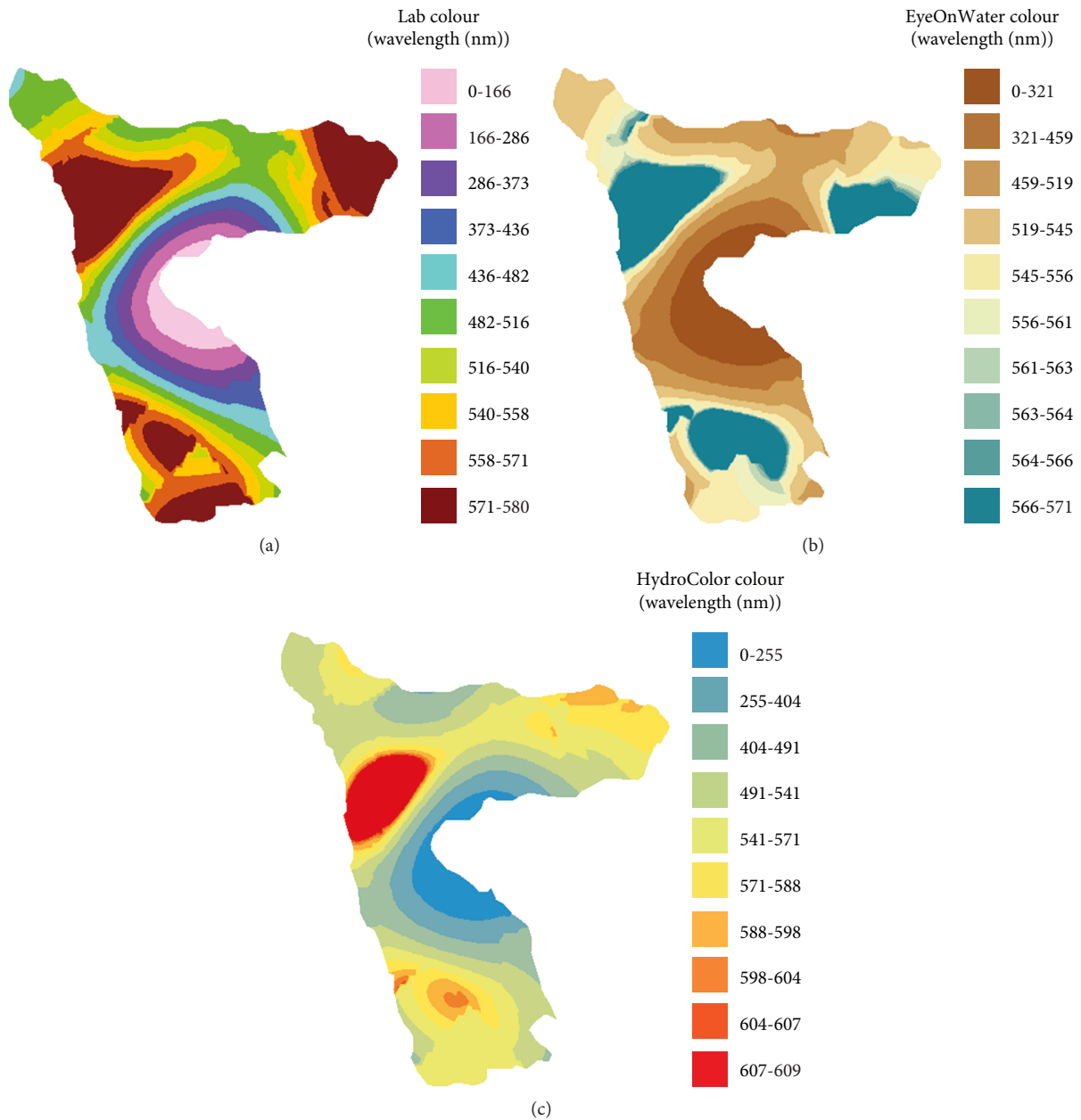


FIGURE 29: Spatially generated water colour variability map from (a) laboratory measurements, (b) EyeOnWater app, and (c) HydroColor app.

from the HydroColor app which uses the RGB colour space. This difference could be attributed to error contribution by the  $x$ -chromaticity coordinate conversion process. For the chlorophyll estimation from the HydroColor app, the adjusted ratio Cchl showed a perfect match for chlorophyll- $a$  estimation and the actual Chl- $a$  was estimated with Pearson's correlation coefficient of  $r > 0.8$ .

The increasing demand for high-resolution spatial and temporal environmental monitoring echoes the need for new and easy-to-use methods for the collection of reliable and accurate data sets for water quality monitoring and control. From the current study results, it is concluded that the evaluated remote sensing models are effective, cheaper, and significant in monitoring freshwater bodies like reservoirs,

as compared to the conventional laboratory measurement. Complemented by predictive algorithms, the smartphone apps are demonstrated to meet the potential requirements of future investigations targeting water quality predictions and serve as potential methodologies for providing timely benchmark information about the aquatic environment to the public, scientists, and policymakers. In order to improve on the reliability and utility of the apps, further studies through seasonal observations, calibration, and validation in different geographically homogeneous case studies will improve and enable standardization of their applicability. Further, in the initial validation process, future studies would consider the simultaneous validation of the app radiances against the satellite sensor-measured radiances for the

derived water quality parameters. This is because the existing empirical algorithms may be subjective and biased to specific geographical region and reservoir water body characteristics.

Further, in order to improve on the water quality retrieval using the smartphones, the knowledge and integration of other measurable environmental variables that contribute to the apparent water colour such as wind speed, cloud cover, location, and accuracy of measurements should be considered towards improving the derivation of the water quality parameters from the smartphone apps. As compared with the traditional sample collection and analysis approaches, the potential advantages of remote sensing sensor-based approaches are demonstrated and can effectively be used for increased spatial-temporal monitoring of reservoirs and for continuous assessment and or management of water quality.

### Data Availability

The author confirms that the data supporting the findings of this study are available within the article.

### Conflicts of Interest

The authors declare that there are no conflicts of interests, regarding the publication of this paper.

### Acknowledgments

This work was compiled when the author was a visiting Research Professor at the HFT Stuttgart in Germany, and the author would like to acknowledge and thank the host, Professor Michael Hahn of HFT Stuttgart, and the Alexander von Humboldt Foundation for the fellowship grant. Paul Okoth is acknowledged for his advice on the development of the extended JavaScript for online EyeOn-Water data processing.

### References

- [1] K. Y. Kondratyev, D. V. Pozdnyakov, and L. H. Pettersson, "Water quality remote sensing in the visible spectrum," *International Journal of Remote Sensing*, vol. 19, no. 5, pp. 957–979, 1998.
- [2] M. Gholizadeh, A. Melesse, and L. Reddi, "A comprehensive review on water quality parameters estimation using remote sensing techniques," *Sensors*, vol. 16, no. 8, pp. 1298–1306, 2016.
- [3] A. G. Dekker, Ž. Zamurović-Nenad, H. J. Hoogenboom, and S. W. M. Peters, "Remote sensing, ecological water quality modelling and in situ measurements: a case study in shallow lakes," *Hydrological Sciences Journal*, vol. 41, no. 4, pp. 531–547, 1996.
- [4] J. C. Ritchie, P. V. Zimba, and J. H. Everitt, "Remote sensing techniques to assess water quality," *Photogrammetric Engineering and Remote Sensing*, vol. 69, no. 6, pp. 695–704, 2003.
- [5] S. Garaba, A. Friedrichs, D. Voß, and O. Zielinski, "Classifying natural waters with the Forel-Ule colour index system: results, applications, correlations and crowdsourcing," *International Journal of Environmental Research and Public Health*, vol. 12, no. 12, pp. 16096–16109, 2015.
- [6] S. Novoa, M. Wernand, and H. J. van der Woerd, "WACODI: a generic algorithm to derive the intrinsic color of natural waters from digital images," *Limnology and Oceanography: Methods*, vol. 13, no. 12, pp. 697–711, 2015.
- [7] M. R. Wernand, A. Hommersom, and H. J. van der Woerd, "MERIS-based ocean colour classification with the discrete Forel-Ule scale," *Ocean Science*, vol. 9, no. 3, pp. 477–487, 2013.
- [8] F. Watanabe, E. Alcântara, T. Rodrigues, N. Imai, C. Barbosa, and L. Rotta, "Estimation of chlorophyll-a concentration and the trophic state of the Barra Bonita hydroelectric reservoir using OLI/Landsat-8 images," *International Journal of Environmental Research and Public Health*, vol. 12, no. 9, pp. 10391–10417, 2015.
- [9] P. A. Brivio, C. Giardino, and E. Zilioli, "Validation of satellite data for quality assurance in lake monitoring applications," *Science of the Total Environment*, vol. 268, no. 1–3, pp. 3–18, 2001.
- [10] S. W. Myint and N. D. Walker, "Quantification of suspended sediments from satellite," *International Journal of Remote Sensing*, vol. 23, no. 16, pp. 3219–3249, 2002.
- [11] P. D. Wass, S. D. Marks, J. W. Finch, G. J. L. Leeks, and J. K. Ingram, "Monitoring and preliminary interpretation of in-river turbidity and remote sensed imagery for suspended sediment transport studies in the Humber catchment," *Science of the Total Environment*, vol. 194–195, pp. 263–283, 1997.
- [12] I. Dor and N. Ben-Yosef, "Monitoring effluent quality in hypertrophic wastewater reservoirs using remote sensing," *Water Science and Technology*, vol. 33, no. 8, pp. 23–29, 1996.
- [13] C. Zuccari Fernandes Braga, A. W. Setzer, and L. Drude de Lacerda, "Water quality assessment with simultaneous Landsat-5 TM data at Guanabara Bay, Rio de Janeiro, Brazil," *Remote Sensing of Environment*, vol. 45, no. 1, pp. 95–106, 1993.
- [14] A. G. Dekker and S. W. M. Peters, "The use of the thematic mapper for the analysis of eutrophic lakes: a case study in the Netherlands," *International Journal of Remote Sensing*, vol. 14, no. 5, pp. 799–821, 1993.
- [15] P. Brezonik, K. D. Menken, and M. Bauer, "Landsat-based remote sensing of lake water quality characteristics, including chlorophyll and colored dissolved organic matter (CDOM)," *Lake and Reservoir Management*, vol. 21, no. 4, pp. 373–382, 2005.
- [16] W. Zhu, Q. Yu, Y. Q. Tian, B. L. Becker, T. Zheng, and H. J. Carrick, "An assessment of remote sensing algorithms for colored dissolved organic matter in complex freshwater environments," *Remote Sensing of Environment*, vol. 140, pp. 766–778, 2014.
- [17] P. N. Mahama, *Assessment of the Utility of Smartphones for Water Quality Monitoring*, [M.S. thesis], ITC Netherlands, 2016.
- [18] K. A. Sudduth, G. S. Jang, R. N. Lerch, and E. J. Sadler, "Long-term agroecosystem research in the Central Mississippi River basin: hyperspectral remote sensing of reservoir water quality," *Journal of Environmental Quality*, vol. 44, no. 1, pp. 71–83, 2015.
- [19] Y. Zhang, S. Lin, J. Liu, X. Qian, and Y. Ge, "Time-series MODIS image-based retrieval and distribution analysis of total suspended matter concentrations in Lake Taihu (China),"

- International Journal of Environmental Research and Public Health*, vol. 7, no. 9, pp. 3545–3560, 2010.
- [20] J. Gregor, R. Geris, B. Marsalek, J. Hetesa, and P. Marvan, “In situ quantification of phytoplankton in reservoirs using a submersible spectrofluorometer,” *Hydrobiology*, vol. 548, no. 1, pp. 141–151, 2005.
- [21] P. Patra, S. K. Dubey, R. K. Trivedi, S. K. Sahu, and S. K. Rout, “Estimation of chlorophyll-*a* concentration and trophic states for an inland lake from Landsat 8 OLI data: a case of Nalban Lake of East Kolkata Wetland, India,” *Preprints*, no. article 2016080149, 2016.
- [22] Z. Zheng, Y. Li, Y. Guo, Y. Xu, G. Liu, and C. Du, “Landsat-based long-term monitoring of total suspended matter concentration pattern change in the wet season for Dongting Lake, China,” *Remote Sensing*, vol. 7, no. 10, pp. 13975–13999, 2015.
- [23] N. Laili, F. Arafah, L. M. Jaelani et al., “Development of water quality parameter retrieval algorithms for estimating total suspended solids and chlorophyll-*A* concentration using Landsat-8 imagery at Poteran island water,” *ISPRS Annals of Photogrammetry, Remote Sensing and Spatial Information Sciences*, vol. II-2/W2, pp. 55–62, 2015.
- [24] E. Alparslan, C. Aydoğan, V. Tufekci, and H. Tüfekci, “Water quality assessment at Ömerli Dam using remote sensing techniques,” *Environmental Monitoring and Assessment*, vol. 135, no. 1–3, pp. 391–398, 2007.
- [25] N. Torbick and M. Corbiere, “A multiscale mapping assessment of Lake Champlain cyanobacterial harmful algal blooms,” *International Journal of Environmental Research and Public Health*, vol. 12, no. 9, pp. 11560–11578, 2015.
- [26] M. T. Waxter, *Analysis of Landsat Satellite Data to Monitor Water Quality Para meters in Tenmile Lake, Oregon, [M.S. thesis]*, Portland State University, 2014.
- [27] Z. Yang and Y. Anderson, “Estimating chlorophyll-*a* concentration in a freshwater Lake using Landsat 8 imagery,” *Journal of Environment and Earth Science*, vol. 6, no. 4, pp. 134–142, 2016.
- [28] A. Friedrichs, J. Busch, H. van der Woerd, and O. Zielinski, “SmartFluo: a method and affordable adapter to measure chlorophyll *a* fluorescence with smartphones,” *Sensors*, vol. 17, no. 4, p. 678, 2017.
- [29] S. Na, J. Park, S. Baek, S. Oh, and J. Park, “Landsat imagery-based water turbidity monitoring in Lake Paldang, Korea,” in *Land Surface Remote Sensing. Proceedings of the SPIE*, vol. 8524, article id 85242H, p. 9, Kyoto, Japan, 2012.
- [30] E. Olet, *Water Quality Monitoring of Roxo Reservoir Using Landsat Images and In-situ Measurements, [M.S. thesis]*, International Institute for Geo-Information Science and Earth Observation, Enschede, The Netherlands, 2010.
- [31] C. Papoutsas and D. G. Hadjimitsis, “Remote sensing for water quality surveillance in inland waters: the case study of Asprokremmos Dam in Cyprus,” in *Remote Sensing of Environment - Integrated Approaches*, pp. 131–153, InTech, 2013.
- [32] J. Busch, R. Bardaji, L. Ceccaroni et al., “Citizen bio-optical observations from coast- and ocean and their compatibility with ocean colour satellite measurements,” *Remote Sensing*, vol. 8, no. 11, p. 879, 2016.
- [33] J. A. Busch, I. Price, E. Jeansou, O. Zielinski, and H. J. van der Woerd, “Citizens and satellites: assessment of phytoplankton dynamics in a NW Mediterranean aquaculture zone,” *International Journal of Applied Earth Observation and Geoinformation*, vol. 47, pp. 40–49, 2016.
- [34] C. Garcia-Soto, G. I. van der Meeren, J. A. Busch et al., “Advancing citizen science for coastal and ocean research,” in *Position Paper 23 of the European Marine Board*, V. French, P. Kellett, J. Delany, and N. McDonough, Eds., p. 112, European Marine Board, Ostend, Belgium, 2017.
- [35] R. Bardaji and J. Piera, “Monitoring marine environments with crowdsourcing methods: water transparency estimation using low cost technologies,” in *3rd EOS Topical Meeting on Blue Photonics. Optics in the Sea (Blue Photonics 3)*, pp. 1–16, Texel, Netherlands, 2013.
- [36] M. R. Wernand, H. J. van der Woerd, and W. W. C. Gieskes, “Trends in ocean colour and chlorophyll concentration from 1889 to 2000, worldwide,” *PLoS One*, vol. 8, no. 6, article e63766, 2013.
- [37] M. A. Eleveld, R. Pasterkamp, H. J. van der Woerd, and J. D. Pietrzak, “Remotely sensed seasonality in the spatial distribution of sea-surface suspended particulate matter in the southern North Sea,” *Estuarine, Coastal and Shelf Science*, vol. 80, no. 1, pp. 103–113, 2008.
- [38] R. J. Davies-Colley and D. G. Smith, “Turbidity suspended sediment, and water clarity: a review,” *Journal of the American Water Resources Association*, vol. 37, no. 5, pp. 1085–1101, 2001.
- [39] G. Wyzeccki and W. S. Stiles, *Colour Science: Concepts and Methods, Quantitative Data, and Formulae*, Wiley, New York, NY, USA, 2nd edition, 1982.
- [40] T. Leeuw, *Crowdsourcing Water Quality Data Using the iPhone Camera*, Fogler Library, Orono, ME, USA, 2014.
- [41] T. Leeuw and E. Boss, “Crowdsourcing water quality data using the iPhone camera,” in *Ocean Science Meeting*, Honolulu, Hawaii, 2014, <http://www.eposters.net/pdfs/crowdsourcing-water-quality-data-using-the-iphone-camera.pdf>.
- [42] M. Whiting, *Turbidity Study for the Union River and a Discussion of Water Level Fluctuations in Graham Lake*, 2017, <https://mainesalmonrivers.org/wp-content/uploads/2017/01/Union-River-Turbidity-Study.pdf>.
- [43] A. I. Dogliotti, K. G. Ruddick, B. Nechad, D. Doxaran, and E. Knaeps, “A single algorithm to retrieve turbidity from remotely-sensed data in all coastal and estuarine waters,” *Remote Sensing of Environment*, vol. 156, pp. 157–168, 2015.
- [44] M. McNeff and A. Mendiratta, *iOcean RGB Sensor*, Cal Poly State University, San Luis Obispo, CA, USA, 2015.
- [45] W. He, S. Chen, X. Liu, and J. Chen, “Water quality monitoring in a slightly-polluted inland water body through remote sensing — case study of the Guanting Reservoir in Beijing, China,” *Frontiers of Environmental Science & Engineering in China*, vol. 2, no. 2, pp. 163–171, 2008.
- [46] T. Lindell, D. Pierson, G. Premazzi, and E. Zilioli, Eds., *Manual for Monitoring European Lakes Using Remote Sensing Techniques*, vol. 18665, Office for Official Publications of the European Communities (EN), Luxembourg, Europe, 1999.
- [47] P. Härmä, J. Vepsäläinen, T. Hannonen et al., “Detection of water quality using simulated satellite data and semi-empirical algorithms in Finland,” *Science of the Total Environment*, vol. 268, no. 1–3, pp. 107–121, 2001.
- [48] E. F. Vermote, D. Tanre, J. L. Deuze, M. Herman, and J. J. Morcette, “Second simulation of the satellite signal in the solar spectrum, 6S: an overview,” *IEEE Transactions on Geoscience and Remote Sensing*, vol. 35, no. 3, pp. 675–686, 1997.
- [49] A. G. Dekker, R. J. Vos, and S. W. M. Peters, “Comparison of remote sensing data, model results and in situ data for total

- suspended matter (TSM) in the southern Frisian lakes,” *Science of the Total Environment*, vol. 268, no. 1-3, pp. 197–214, 2001.
- [50] Y. Ouma, “Evaluation of multiresolution digital elevation model (DEM) from real-time kinematic GPS and ancillary data for reservoir storage capacity estimation,” *Hydrology*, vol. 3, no. 2, p. 16, 2016.
- [51] S. M. Kloiber, P. L. Brezonik, L. G. Olmanson, and M. E. Bauer, “A procedure for regional lake water clarity assessment using Landsat multispectral data,” *Remote Sensing of Environment*, vol. 82, no. 1, pp. 38–47, 2002.
- [52] M. A. Reddy, “A detailed statistical study on selection of optimum IRS LISS pixel configuration for development of water quality models,” *International Journal of Remote Sensing*, vol. 18, no. 12, pp. 2559–2570, 1997.
- [53] B. Nas, S. Ekerin, H. Karabork, A. Berktaç, and D. J. Mulla, “An application of Landsat-5TM image data for water quality mapping in Lake Beyşehir, Turkey,” *Water, Air, & Soil Pollution*, vol. 212, no. 1-4, pp. 183–197, 2010.
- [54] C. Gemperli, *Determination of Water Quality Parameters in Indian Ponds Using Remote Sensing Methods*, University of Zurich, Zurich, Switzerland, 2004.
- [55] F. Bilge, B. Yazici, T. Dogeroglu, and C. Ayday, “Statistical evaluation of remotely sensed data for water quality monitoring,” *International Journal of Remote Sensing*, vol. 24, no. 24, pp. 5317–5326, 2003.
- [56] A. G. Dekker, R. J. Vos, and S. W. M. Peters, “Analytical algorithms for lake water TSM estimation for retrospective analyses of TM and SPOT sensor data,” *International Journal of Remote Sensing*, vol. 23, no. 1, pp. 15–35, 2002.
- [57] F. Wang, L. Han, H. T. Kung, and R. B. van Arsdale, “Applications of Landsat-5 TM imagery in assessing and mapping water quality in Reelfoot Lake, Tennessee,” *International Journal of Remote Sensing*, vol. 27, no. 23, pp. 5269–5283, 2006.
- [58] E. L. Hestir, V. E. Brando, M. Bresciani et al., “Measuring freshwater aquatic ecosystems: the need for a hyperspectral global mapping satellite mission,” *Remote Sensing of Environment*, vol. 167, pp. 181–195, 2015.
- [59] H. Van der Werff and F. van der Meer, “Sentinel-2A MSI and Landsat 8 OLI provide data continuity for geological remote sensing,” *Remote Sensing*, vol. 8, no. 11, p. 883, 2016.
- [60] D. Barrett and A. Frazier, “Automated method for monitoring water quality using Landsat imagery,” *Water*, vol. 8, no. 6, p. 257, 2016.
- [61] T. Cooley, G. P. Anderson, G. W. Felde et al., “FLAASH, a MODTRAN4-based atmospheric correction algorithm, its application and validation,” in *IEEE International Geoscience and Remote Sensing Symposium*, pp. 1414–1418, Toronto, ON, Canada, 2002.
- [62] Y. J. Kaufman, A. E. Wald, L. A. Remer, Bo-Cai Gao, Rong-Rong Li, and L. Flynn, “The MODIS 2.1- $\mu\text{m}$  channel-correlation with visible reflectance for use in remote sensing of aerosol,” *IEEE Transactions on Geoscience and Remote Sensing*, vol. 35, no. 5, pp. 1286–1298, 1997.
- [63] G. A. Maul, *Introduction to Satellite Oceanography*, Martinus Nijhoff Publishers, Boston, MA, USA, 1985.
- [64] H. R. Gordon, “Calibration requirements and methodology for remote sensors viewing the ocean in the visible,” *Remote Sensing of Environment*, vol. 22, no. 1, pp. 103–126, 1987.
- [65] S. Novoa, M. R. Wernand, and H. J. van der Woerd, “The Forel-Ule scale revisited spectrally: preparation protocol, transmission measurements and chromaticity,” *Journal of the European Optical Society: Rapid Publications*, vol. 8, article 13057, 2013.
- [66] S. Novoa, M. R. Wernand, and H. J. . . Woerd, “The modern Forel-Ule scale: a ‘do-it-yourself’ colour comparator for water monitoring,” *Journal of the European Optical Society: Rapid Publications*, vol. 9, article 14025, 2014.
- [67] S. Westland, C. Ripamonti, and V. Cheung, *Computational Colour Science Using MATLAB®*, Wiley, 2012.
- [68] D. Pascale, *A Review of RGB Color Spaces*, The Babel Color Company, Montreal, QC, USA, 2003.
- [69] G. Neukermans, K. G. Ruddick, and N. Greenwood, “Diurnal variability of turbidity and light attenuation in the southern North Sea from the SEVIRI geostationary sensor,” *Remote Sensing of Environment*, vol. 124, pp. 564–580, 2012.
- [70] W. Luo, M. C. Taylor, and S. R. Parker, “A comparison of spatial interpolation methods to estimate continuous wind speed surfaces using irregularly distributed data from England and Wales,” *International Journal of Climatology*, vol. 28, no. 7, pp. 947–959, 2008.
- [71] R. R. Murphy, F. C. Curriero, and W. P. Ball, “Comparison of spatial interpolation methods for water quality evaluation in the Chesapeake Bay,” *Journal of Environmental Engineering*, vol. 136, no. 2, pp. 160–171, 2010.
- [72] M. G. D. Obarrio, *Water Quality and Its Spatial Variability in Lake Cuitzeo, Mexico, [M.S. thesis]*, ITC Netherlands, 2005.
- [73] Y. O. Ouma, T. Owiti, E. Kipkorir, J. Kibiiy, and R. Tateishi, “Multitemporal comparative analysis of TRMM-3B42 satellite-estimated rainfall with surface gauge data at basin scales: daily, decadal and monthly evaluations,” *International Journal of Remote Sensing*, vol. 33, no. 24, pp. 7662–7684, 2012.
- [74] L. S. Gandin, *Objective Analysis of Meteorological Fields*, Gidrometeorologicheskoe-Izdatelstvo (G MIZ), 1963.
- [75] G. Matheron, “Principles of geostatistics,” *Economic Geology*, vol. 58, no. 8, pp. 1246–1266, 1963.
- [76] N. Cressie, “Kriging nonstationary data,” *Journal of the American Statistical Association*, vol. 81, no. 395, pp. 625–634, 1986.
- [77] J. S. Ryu, M. S. Kim, K. J. Cha, T. H. Lee, and D. H. Choi, “Kriging interpolation methods in geostatistics and DACE model,” *KSME International Journal*, vol. 16, no. 5, pp. 619–632, 2002.
- [78] A. G. Journel and C. J. Huijbregts, *Mining Geostatistics*, Academic Press, London, UK, 1978.
- [79] E. H. Isaaks and R. M. Srinivasta, *Applied Geostatistics*, Oxford University Press, Oxford, UK, 1989.
- [80] D. W. Wong, L. Yuan, and S. A. Perlin, “Comparison of spatial interpolation methods for the estimation of air quality data,” *Journal of Exposure Analysis and Environmental Epidemiology*, vol. 14, no. 5, pp. 404–415, 2004.
- [81] J. A. Mulholland, A. J. Butler, J. G. Wilkinson, A. G. Russell, and P. E. Tolbert, “Temporal and spatial distributions of ozone in Atlanta: regulatory and epidemiologic implications,” *Journal of the Air & Waste Management Association*, vol. 48, no. 5, pp. 418–426, 1998.
- [82] L. P. Vernon, “Spectrophotometric determination of chlorophylls and pheophytins in plant extracts,” *Analytical Chemistry*, vol. 32, no. 9, pp. 1144–1150, 1960.
- [83] O. Zielinski, J. A. Busch, A. D. Cembella et al., “Detecting marine hazardous substances and organisms: sensors for pollutants, toxins, and pathogens,” *Ocean Science*, vol. 5, no. 3, pp. 329–349, 2009.

- [84] H. Duan, Y. Zhang, B. Zhang, K. Song, and Z. Wang, "Assessment of chlorophyll-a concentration and trophic state for Lake Chagan using Landsat TM and field spectral data," *Environmental Monitoring and Assessment*, vol. 129, no. 1-3, pp. 295-308, 2007.
- [85] A. Kulkarni, "Water quality retrieval from Landsat TM imagery," *Procedia Computer Science*, vol. 6, pp. 475-480, 2011.
- [86] W. Ma, Q. Xing, C. Chen, Y. Zhang, D. Yu, and P. Shi, "Using the normalized peak area of remote sensing reflectance in the near-infrared region to estimate total suspended matter," *International Journal of Remote Sensing*, vol. 32, no. 22, pp. 7479-7486, 2011.
- [87] K. S. Song, D. M. Lu, D. W. Liu et al., "Retrival of total suspended matter (TSM) using remotely sensed images in Shitoukoumen Reservoir, Northeast China," in *2010 IEEE International Geoscience and Remote Sensing Symposium*, pp. 405-408, Honolulu, HI, USA, July 2010.
- [88] B. Zhang, J. Li, Q. Shen, and D. Chen, "A bio-optical model based method of estimating total suspended matter of Lake Taihu from near-infrared remote sensing reflectance," *Environmental Monitoring and Assessment*, vol. 145, no. 1-3, pp. 339-347, 2008.
- [89] J. P. Xu, B. Zhang, K. S. Song et al., "Bio-optical model of total suspended matter based on reflectance in the near infrared wave band for case-II waters," *Spectroscopy and Spectral Analysis*, vol. 28, no. 10, pp. 2273-2277, 2008.
- [90] M. Onderka and P. Pekárová, "Retrieval of suspended particulate matter concentrations in the Danube River from Landsat ETM data," *Science of the Total Environment*, vol. 397, no. 1-3, pp. 238-243, 2008.
- [91] D. Doxaran, J.-M. Froidefond, S. Lavender, and P. Castaing, "Spectral signature of highly turbid waters: application with spot data to quantify suspended particulate matter concentrations," *Remote Sensing of Environment*, vol. 81, no. 1, pp. 149-161, 2002.
- [92] M. Dihkan, F. Karsli, and A. Guneroglu, "Mapping total suspended matter concentrations in the Black Sea using Landsat TM multispectral satellite imagery," *Fresenius Environmental Bulletin*, vol. 20, pp. 262-269, 2011.
- [93] B. J. Hicks, G. A. Stichbury, L. K. Brabyn, M. G. Allan, and S. Ashraf, "Hindcasting water clarity from Landsat satellite images of unmonitored shallow lakes in the Waikato region, New Zealand," *Environmental Monitoring and Assessment*, vol. 185, no. 9, pp. 7245-7261, 2013.
- [94] M. K. Grove, G. S. Bilotta, R. R. Woockman, and J. S. Schwartz, "Suspended sediment regimes in contrasting reference-condition freshwater ecosystems: implications for water quality guidelines and management," *Science of the Total Environment*, vol. 502, pp. 481-492, 2015.
- [95] C. F. Cerco, S. C. Kim, and M. R. Noel, "Management modeling of suspended solids in the Chesapeake Bay, USA," *Estuarine, Coastal and Shelf Science*, vol. 116, pp. 87-98, 2013.





**Hindawi**

Submit your manuscripts at  
[www.hindawi.com](http://www.hindawi.com)

